In situ electric field diagnostics using xenon stark spectroscopy

Visser, B.

Award date:
2002

Master Thesis

In Situ Electric Field Diagnostics Using Xenon Stark Spectroscopy

Bram Visser

Elementary Processes in Gasdischarges (EPG)

supervisors:
dr. M. D. Bowden
prof. dr. ir. G. M. W. Kroesen

February 2002

Abstract

The electric field in a plasma is an important quantity but in situ measurement is often difficult due to the lack of suitable measurement techniques. This is particularly true for measurement in lighting plasmas such as discharge lamps and plasma display panels. In this thesis, we report the development of a new method for the measurement of electric fields in glow discharge plasmas, based on Stark spectroscopy of xenon atoms. A key feature of the method is that the electric field is determined by matching experimentally obtained absorption spectra to theoretically calculated spectra. Measurements of Stark spectra are made in the sheath region of a glow discharge using laser spectroscopy. These measurements are compared with theoretical spectra, calculated by solving the Schrödinger equation for the case of a xenon atom in the presence of an electric field. In this thesis, results of preliminary spectra will be presented and the suitability of different excitation schemes will be discussed.

Contents

Chapter 1

Introduction

Glow discharges are very much present in our everyday lives, from the plasma television at home to the fluorescent lights in the office. In addition, they are widely used in material processing, in applications such as etching and deposition. In order to predict processes in glow discharges, fundamental properties have to be modelled, diagnosed and understood. In recent decades, a lot of work has been done in modelling glow discharges but all these models struggle with one problem, the boundary. Discharges can have large gradients in properties such as electric field, electron density and average electron energy at the boundary. Relating these properties to bulk plasma parameters remains a challenge. The need to pick up this challenge is related to the fact that many of the applications that use glow discharges very much depend on behavior at the boundary. In order to understand processes at the boundary, parameters have to be measured. One of the parameters that is a driving force behind many processes at the boundary is the electric field. In many cases, electric fields can be estimated with reasonable accuracy. In some cases, though, and especially in a dynamic discharge, this becomes increasingly difficult.

In recent years, glow discharges containing xenon are used in applications as UV light sources. One application that uses xenon as an UV light source is a Plasma Display Panel (PDP). Each pixel (PDP cell) contains a xenon microdischarge for the generation of UV-photons, which are used to excite a phosphor located on the walls of the cell. Visible light (red, green and blue) is generated when the excited phosphor relaxes to the ground state. Building an image every refreshing cycle of the PDP requires pulsed operation of the microdischarge. The main technology problem of these displays is the poor light efficacy. The energy put in this microdischarge is not very efficiently converted to UV photons due to several loss mechanisms. One of the major loss mechanisms predicted by models [1] is the loss of ions which are accelerated to the walls. The electric field present in the discharge drives this process and experimental data is needed to verify this. Therefore an in situ diagnostic would be welcome to measure the electric fields in this discharge.

Throughout the years, measuring electric fields correctly has proved to be difficult but methods have been developed. The first type of diagnostic which comes to mind is electrical probes. The main problem with the use of probes is the fact they induce perturbations, either by their geometrical presence or by the fact they emit or absorb charged particles. Both effects change the electric field, around the probe, which makes the interpretation of measurements not straightforward. The application of probes in microdischarges like PDP cells is not feasible and will not be pursued for the development of electric field diagnostic in this thesis, although probes are used in many other applications with success [2, 3].

Measuring emission could be a second possibility to develop an electric field diagnostic. Methods based on emission are passive. They are non-perturbative and in addition can also give good spatial and temporal resolution. Energy levels of atoms/molecules start mixing due to the presence of electric fields. This can cause several observable effects. For example, the mixing of adjacent states can cause normally forbidden transitions to become partially allowed. Degenerate levels can split into separate energy states. Mixing can also shift levels which can be observed as a change in transition wavelength. All these Stark effects can be used to measure electric fields. Previous research [4, 5, 6] shows that, in order to be able

to obtain some electric field resolution, the electric field has to be at least 1.5 kV/cm and in most cases several hundreds of kV/cm. Electric field strengths in a PDP discharge are roughly about 0-4 kV/cm. Only being able to measure above 1.5 kV/cm or much higher makes this not a feasible option to develop an electric field diagnostic.

An active method that makes use of Stark effects to measure electric fields is laser spectroscopy. For highly excited states the influence of electric field is larger and Stark effects are observed more easily. To probe these highly excited states high energy lasers are required. Directing a high energy laser in a discharge might induce charges which perturb the electric field. But in general laser spectroscopy is considered non-perturbative, because either the electric field is disturbed on time scales longer then the time the laser is present or the effect is small enough to be neglected.

During the last 25 years, several laser based Stark spectroscopy methods have been developed to measure electric field. The first laser based Stark spectroscopy method was described by Moore *et al.* [7], who related the appearance of forbidden lines in the laser induced fluorescence spectrum of BCl to electric field strength. This Stark spectroscopy method, later also applied to NaK [8], requires the presence of BCl molecules in the discharge. BCl molecules can form negative ions and, even in small densities, change the discharge properties significantly.

A different Stark spectroscopy method was developed by Doughty *et al.* [9] by excitation of highly excited states in helium. These highly excited states of helium are hydrogen-like and are therefore called Rydberg states. The Stark effects for Rydberg states of helium were calculated, based on theory described by, for example Salpether and Bethe [30]. Hydrogen also was used to measure electric field [10] in a similar way, by relating theory and observed Stark effects. The Doughty method could very successfully be applied to measure electric fields at the boundary of rf discharges [11, 12, 13], showing the capability of high temporal resolution. A disadvantage of Doughty's method was that an opto-galvanic method was used to detect the excitation to highly excited states. The opto-galvanic method detects excitation by the change of the impedance due to laser light passing through the discharge, giving a line integrated signal. The lack of spatial resolution and the dependence on stability of the impedance limits the application of Doughty's method. In 1996, first electric field measurements were reported by Stark spectroscopy on the argon atom by Choi *et al.* [14]. This argon method was calibrated experimentally by determining the electric field at the boundary of a negative glow discharge with helium and relating the field strength to the obtained Stark spectra of argon. Excitation to the Rydberg states was also detected by collisional induced fluorescence solving the spatial resolution problem of Doughty's method. Later Gavrilenko *et al.* [15] calculated the argon spectra by applying a calculation method described previously by Zimmerman *et al.* [16] improving the electric field resolution to 140 V/cm.

The methods mentioned in the paragraph above have one limitation. Because it was not possible to excite from the ground state to a Rydberg state with the laser systems that were used, all excitations were achieved from a metastable level. In some regions of the discharge the population of metastable levels is not sufficient to allow electric field measurements. The method with the best electric field resolution (5 V/cm) so far, described by Czarnetski *et al.* [18] and based on hydrogen, solved this problem. Czarnetski's method uses two lasers with one laser preparing an intermediate state by two photon excitation from the ground state and the second laser exciting from the prepared state to highly excited levels. Excitation to the highly excited levels is detected by a dip in the fluorescence, from the intermediate state.

It can be seen in the above discussion that there are possibilities to actively measure electric field in a discharge, but not for the gas species present in a PDP. The aim of the research presented in this thesis was, therefore, to develop a method to measure electric fields by laser based Stark spectroscopy of xenon atoms. This diagnostic was designed to provide the possibility to meet the spatial and temporal resolution needed to measure electric fields in a PDP cell. The method had to have two important features. First, the experimental Stark spectra of xenon had to be obtained in a similar way as Czarnetski did for hydrogen and Choi for argon. The second feature was the theoretical calculation of Stark effects on xenon in the same way as Gavrilenko did for argon. This thesis describes the first steps in the development of this new method. By using laser spectroscopy the xenon Stark effects are measured in a negative DC glow

discharge. The electric field strength will be determined by comparison with theoretically calculated spectra.

Chapter two introduces the physics describing electric fields in glow discharges. Theory to calculate Stark effects and calculation results for xenon are presented in chapter three. Experimental schemes and set-ups used to develop the xenon method are outlined in chapter four. Chapter five contains the experimentally obtained spectra and compares them to the theoretical spectra calculated in chapter three. A conclusion, prospects and recommendations are given in chapter six.

Chapter 2

Electric Fields in DC Glow Discharges

This chapter tries to outline some of the physics determining how the electric field distributes in a discharge. A more thorough review can be found in e.g the book of Chapman [19]. For the development of the electric field diagnostic, a stable type of discharge was necessary and a negative DC glow discharge was chosen. Therefore, in the first section this type of discharge is explained. In the second section, the electric fields in the boundary region of the DC glow discharge are discussed.

2.1 DC Glow Discharge

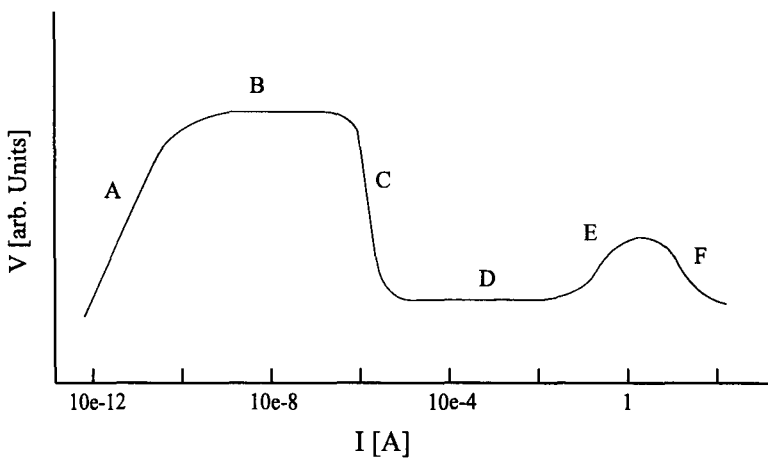

Fig. 2.1: Voltage as a function of current characteristic for a discharge. (A) Before breakdown region. (B) Townsend discharge region. (C) Transition region with negative voltage current characteristic. (D) glow region. (E) anomalous glow region. (F) arcing region.

When a potential difference (voltage) is applied across a gas a discharge can occur. In Figure (2.1) the voltage-current characteristic is displayed for such a process. In the first region (A), there is a small number of charged particles in the gas and the voltage can be increased without the current increasing substantially. The pressure of the gas and the distance between the electrodes determines the breakdown voltage. When this voltage is reached the gas will breakdown and move into the stable Townsend regime (B). An unstable region (C) can occur caused by space charge and local high electric fields. This region is characterized by a sharp fall in voltage with increasing current. This instability can become worse without limitation of the current by an external circuit. With the increase of current a second stable region is reached called the glow region (D). The glow region takes its name from the glow that appears above the cathode (negative electrode) in the discharge. Before having large enough current to arc between

the electrodes (F) the discharge passes through the anomalous glow region (E). The discharge used to validate the electric field diagnostic described in this report was operated in the glow region.

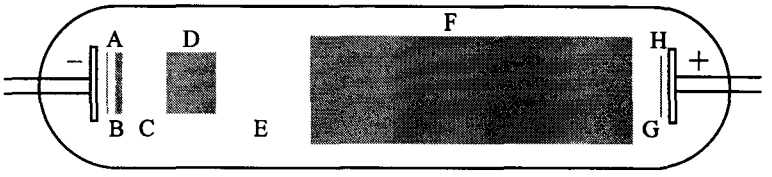

Fig. 2.2: Schematic normal glow discharge in neon in a 50 cm tube at 1 Torr. The luminous regions are shaded. (A) are the cathode layers, (D) the negative glow, (F) the positive column and (H) the anode glow. Dark regions have no shading. (B) is the Aston , (C) the cathode, (E) the Faraday and (G) the anode dark space.

In Figure (2.2) the luminous regions of a glow discharge are illustrated for a neon DC discharge inside a fluorescence tube. Besides several of these glow regions there are dark spaces. The part most representing a plasma is the positive column, the rest is considered a highly not ideal plasma. If we decrease the space between the electrodes the positive column will decrease and eventually disappear. The negative glow and the Faraday dark space will remain as well as two dark regions in front of the electrodes, called sheaths. This type of discharge is called a negative DC glow discharge. The potential distribution can roughly be illustrated by Figure (2.3). The plasma between the electrodes has a constant positive potential φ_p. This is not the intermediate potential between the plates as might be expected but a constant potential higher then the anode potential. The total voltage drop is limited to the sheaths at each of the electrodes. The next sections will give a more detailed description of those regions.

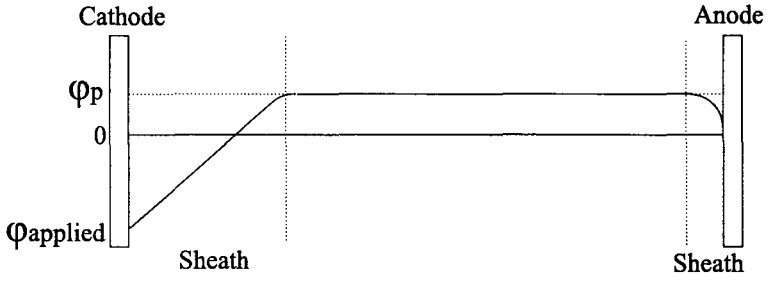

Fig. 2.3: Illustration of the potential distribution across a DC glow discharge.

2.2 Estimating the Plasma Potential

To get an idea of the electric fields present in the cathode sheath of a negative DC glow discharge the potential of the discharge should be considered first. The voltage across the discharge was shown to be entirely over the sheaths. Also the potential of the plasma was above the anode potential and constant. This implies there is no electric field in this region. All this seems to be a contradictory and counter-intuitive. But there is a basic property of plasma causing this behavior. In a plasma there are an equal number of positive as negative charges. The quasi-neutrality and the large number of charged particles equips the plasma to compensate for external electric fields. If charges are separated by an electric field they induce an electric field in the exact opposite direction as the externally applied field, as is shown in Figure (2.4). This effect, called Debye shielding, is characterised by the Debye length:

$$\lambda_D = 7450 \cdot \sqrt{\frac{T_e}{n_e}} \tag{2.1}$$

In this formula λ_D is the Debye length, T_e the electron temperature expressed in eV and n_e the electron density. On a length scale larger than the Debye length, the plasma can compensate for external electric fields, which results in a zero electric field. This can only be disturbed by introducing a floating potential like a wall or electrode.

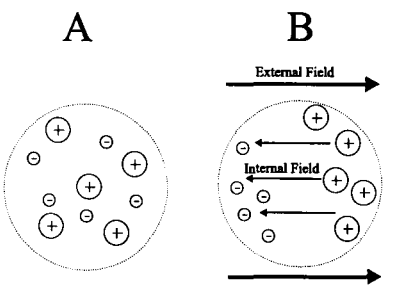

Fig. 2.4: The Debye shielding in a plasma is illustrated. The dashed circle indicates the Debye sphere. In situation (A) there is no electric field while in situation (B) an external electric field is applied

If we want to estimate the electric field in front of the cathode the plasma potential should be estimated. This can be done in a relative simple way, outlined below. Consider a non-grounded wall having a floating potential φ_f in comparison with the discharge. The mean velocity $\sqrt{\frac{8k_BT}{\pi m}}$ is much greater for electrons then for ions, and so more negatively charged electrons will reach the wall then the slower moving ions. This results in a negative charging of the wall. The φ_f of the wall will become negative compared to the potential of the discharge φ_p repelling the electrons and attracting the positive ions. This process will continue until the flux of the positive and the negative charges are equal. No net charge is added anymore but the wall remains negatively charged compared with the discharge. For the electrons there is a potential barrier and ions are accelerated to the wall. This potential barrier for electrons decreases the density of the electrons near the wall. This lower density of electrons means that less excitation of atoms can occur and this region can be clearly seen as a dark space in front of the wall. Recombination and the resulting glow is proportional to the electron density. This space is called the sheath of the discharge. Because there is no Debye shielding this part of the discharge is positively charged.

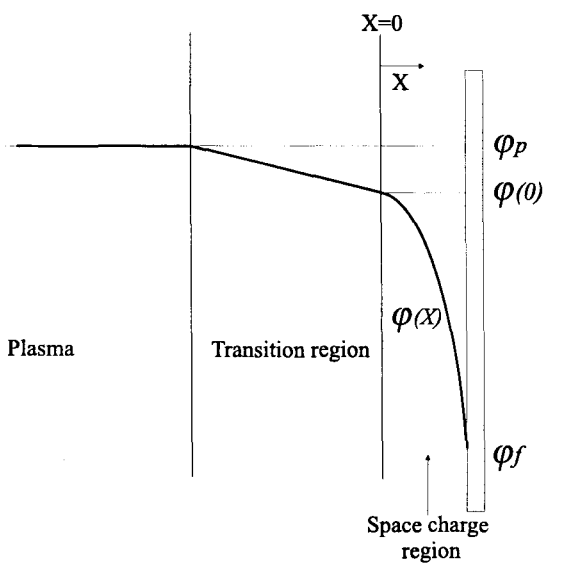

Fig. 2.5: Sheath potential as function of the distance to the cathode

The potential difference of the wall and the plasma can be estimated. In Figure (2.5) the schematic potential is drawn for a sheath. There are two regions to be considered, the quasi-neutral transition region and the positive space charge region. The existence of the low electric field transition region was first proposed by Bohm. This transition region resulting in a higher velocity for entering ions lead to the Bohm sheath criterion and a definition of sheaths edges. The net current to the wall with the floating potential must be zero. Also the ion density has to decrease less rapidly than the electron density in the sheath, because this region is positively charged. These conditions can be matched if the ions enter the positive space charge region with a velocity larger than zero. The next paragraph describes the mathematical equations showing this behavior.

To simplify the calculation the sheath is presumed to be collisioness. All the ions entering the sheath will reach the wall. From conservation of energy $n_i(X)$ can be calculated to be:

$$n_i(X) = n_i(0)\left(1 - \frac{2e[\varphi(X) - \varphi(0)]}{m_i(u(0))^2}\right)^{-1/2} \tag{2.2}$$

n_i is the ion density, e the elementary charge, m_i the mass of the ions, $\varphi(X)$ and $\varphi(0)$ the potentials defined in Figure 2.5, $u(0)$ is the velocity of the ions entering the positive space charge region. From the Boltzman relation follows the electron density $n_e(X)$:

$$n_e(X) = n_e(0)\exp\left[\frac{e[\varphi(X) - \varphi(0)]}{k_B T_e}\right] \tag{2.3}$$

The voltage across the sheath can now be calculated by using Poisson's equation and applying boundary conditions:

$$\frac{d^2\varphi}{dx^2} = \frac{e}{\varepsilon_0}(n_e(X) - n_i(X)) \tag{2.4}$$

Imposing the fact that the space charge region contains positive charge ($\frac{d^2\varphi}{dx^2} \leq 0$), the Bohm criterium can be derived:

$$\exp\left[-\frac{2e[\varphi(X) - \varphi(0)]}{k_B T_e}\right] > 1 - \frac{2e[\varphi(X) - \varphi(0)]}{m_i u(0)^2} \tag{2.5}$$

In the region where $\varphi(X) - \varphi(0)$ is small compared to $k_B T_e$ the exponential can be expanded. From this follows the Bohm criterion:

$$u(0) > \left(\frac{k_B T_e}{m_i}\right)^{1/2} \tag{2.6}$$

This criterion shows the coupling between the movement of electrons and ions in a discharge. In order to have a stable sheath this criterion has to be matched. By assuming the ion velocity inside the plasma zero the potential $\varphi(0)$ has to be $\frac{k_B T_e}{2e}$ lower then the plasma potential. Using this in combination with the boundary condition $n_i(0) = n_e(0)$ the flux of ions in the space charge region is:

$$n_i(0)u(0) \approx 0.6 n_e\left(\frac{k_B T_e}{m_i}\right)^{1/2} \tag{2.7}$$

With this and the condition of no net current when the sheath is stable:

$$\left(n_e \exp\left[-\frac{e(\varphi_p - \varphi_f)}{k_B T_e}\right]\right)\frac{c_e}{4} = n_i 0.6\left(\frac{k_B T_e}{m_i}\right)^{1/2} \tag{2.8}$$

where $c_e = \sqrt{\frac{8k_B T_e}{\pi m_e}}$ is the mean velocity of the electrons. Substituting this results in the voltage $\varphi_p - \varphi_f$ across the sheath can be estimated as:

$$\varphi_p - \varphi_f = \frac{k_B T_e}{2e} \ln\left(\frac{m_i}{2.3 m_e}\right) \tag{2.9}$$

For an Argon plasma with an electron temperature of 2 eV this is estimated to be in the order of 10 V. The voltage drop across in the cathode sheath is then voltage applied between the electrodes plus the plasma potential as illustrated in Figure (2.3).

2.3 Electric Field Distribution in the Sheath

In Figure (2.3) the potential in the sheath drops linearly. This assumes the electric field to be constant across the sheath making this region not very well suited for the validation of an electric field diagnostic. This section will refine this picture by introducing the problem of modelling the boundary and the plasma together, called the bounded plasma problem, and actually calculating the electric distribution in the sheath qualitatively. Sternberg and Godyak [21] evaluated the static bounded plasma problem and this section will use the approach used in their article to show how the profile of the electric field in the sheath is expected to be.

The plasma observed in this thesis is weakly ionized and heat transfer will be neglected. For simplification, the sheath is assumed to be collisionless, although for the discharge used in this thesis this is not entirely the case. The mean free path for ions is in the order of 10 μm and the typical sheath width is in the order of 1 mm. To give a qualitative picture of the electric field distribution in the sheath it is not necessary to include these collisions. This would only give modifications in the absolute sheath width and electric field strength, not in the general appearance of the distribution.

In general the following hydrodynamic equations for ions and electrons can be used to describe a bounded plasma:

$$m_i v_i \nabla v_i + e\nabla\varphi + \frac{k_B T_i}{n_i}\nabla n_i + m_i z v_i \frac{n_e}{n_i} + F_i = 0 \tag{2.10}$$

$$m_e v_e \nabla v_e - e\nabla\varphi + \frac{k_B T_e}{n_e}\nabla n_e + m_e z v_e + F_e = 0 \tag{2.11}$$

$$\nabla(n_i v_i) = z n_e \tag{2.12}$$

$$\nabla(n_e v_e) = z n_e \tag{2.13}$$

$$\Delta\varphi = 4\pi e(n_e - n_i) \tag{2.14}$$

With m_i, m_e the masses, v_i, v_e, the velocities, T_i, T_e, the temperatures and n_i, n_e the densities of the ions and electrons. F_i is the frictional force between the ions and the gas atoms. The frictional force for the electrons is F_e. Boltzman constant is k_B and the elementary charge e. The potential is given by φ. z is the ionization frequency (number of ions created per second by one electron). To obtain a qualitative distribution the Equations (2.10-2.14) need to be normalized. This is done by introducing the following variables:

$$
\begin{aligned}
x &= zr\left(\frac{k_B T_e}{m_i}\right)^{-1/2} \\
u &= v_i\left(\frac{k_B T_e}{m_i}\right)^{-1/2} \\
y &= \frac{n_i}{n_0}, \quad y_e = \frac{n_e}{n_0} \\
\tau &= \frac{T_i}{T_e}, \quad \eta = -\frac{e\varphi}{k_B T_e} \\
\beta &= \frac{F_p\left(\frac{k_B T_e}{m_i}\right)^{-1/2}}{m_i z}
\end{aligned}
\tag{2.15}
$$

It might be noticed the scaling factor used is the Bohm velocity discussed in the previous section (Equation (2.6)). The spatial variable is r with $r = 0$ specifying the center of the plasma and $r = R$ the electrode at distance R. Using the Boltzman equation for the electrons (Equation 2.3) and introducing the non-neutrality parameter $q_0 = \frac{\lambda_{D_0}}{R}$, where $\lambda_{D_0} = \left(\frac{k_B T_e}{4\pi e^2 n_0}\right)^{1/2}$ is the electron Debye length at the center of the plasma, the system can be reduced to the following system:

$$y_e = \exp(-\eta) \tag{2.16}$$

$$\frac{d}{dx}(uy) = y_e \tag{2.17}$$

$$\frac{d}{dx}(\frac{1}{2}u^2 - \eta + \tau \ln y) + u(\frac{y_e}{y}) + \beta(u) = 0 \tag{2.18}$$

$$\frac{d^2\eta}{dx^2} = (q_0 x_w)^{-2}(y - y_e) \tag{2.19}$$

The position of the wall is specified by x_w. The fraction of electrons compared to the neutrals exponentially decays with a Boltzman factor. The flux of ions becomes constant, as expressed in the second equation. The third equation contains the forces experienced by the ions. Finally Poisson's law is described by the last equation. The boundary conditions which can be applied are:

$$
\begin{aligned}
y(0) = 1, \quad u(0) = 0 \\
\eta(0) = 0, \quad \frac{d\eta}{dx}(0) = 0
\end{aligned}
\tag{2.20}
$$

We make the following assumptions: $n_e = n_i = n_0$ at the center; the velocity of the ions v_i is zero at the center; the potential φ is zero; and constant at the center of the plasma. For weakly ionized plasmas, τ is assumed to be zero and the simplification of collisionless sheath makes β zero. For this specific case the system can be rewritten as a set of first-order differential equations:

$$\frac{d\eta}{dx} = \psi \tag{2.21}$$

$$\frac{dy}{dx} = -\frac{y\psi}{u^2} + \frac{2e^{-\eta}}{u} \tag{2.22}$$

$$\frac{du}{dx} = \frac{\psi}{u} - \frac{e^{-\eta}}{y} \tag{2.23}$$

$$\frac{d\psi}{dx} = (q_0 x_w)^{-2}(y - e^{-\eta}) \tag{2.24}$$

Where ψ is the normalized electric field. The solution for the electric field will depend on q_0 which makes it not universal. This set of equations can not be solved analytically and a singularity at the center of the plasma makes solving numerically difficult. Therefore in literature it is more common to separate the sheath model from the plasma model and match them together afterwards. In the sheath model the electron density is assumed to be zero and in the plasma model quasi-neutrality is assumed. The problem which arises here is the choice of the boundary condition for the sheath and the plasma model (see Figure 2.6).

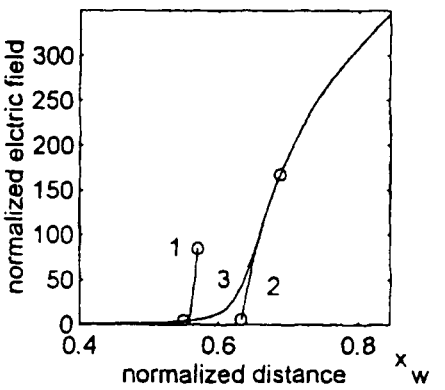

Fig. 2.6: Normalized electric field distribution as a function of the normalized distance from the center of the plasma. (1) Plasma model, (2) Sheath model and (3) the Sternberg Godyak model. [21]

It relies on the definition of where the sheath starts. In the previous section, an estimation was made by using the point where ions have the Bohm velocity. Sternberg and Godyak showed the introduction of the transition region where ion enter with a velocity a little bit lower and leave with a velocity larger then the Bohm velocity. The main conclusion concerning this thesis is the almost linear distribution of electric field strength in the sheath of a negative glow discharge allows experimental validation of an electric field diagnostic in this type of discharge.

Chapter 3

Theory of Xenon Stark Spectroscopy

To calculate Stark effects and relate them to electric field is one of the main features a xenon electric field diagnostic should possess. In the first section the Stark spectroscopy method is described. The theory to calculate Stark effects is outlined in the second section and results of this calculation for xenon will be presented in the third section.

3.1 Electric Field Measurements Using Stark Spectroscopy

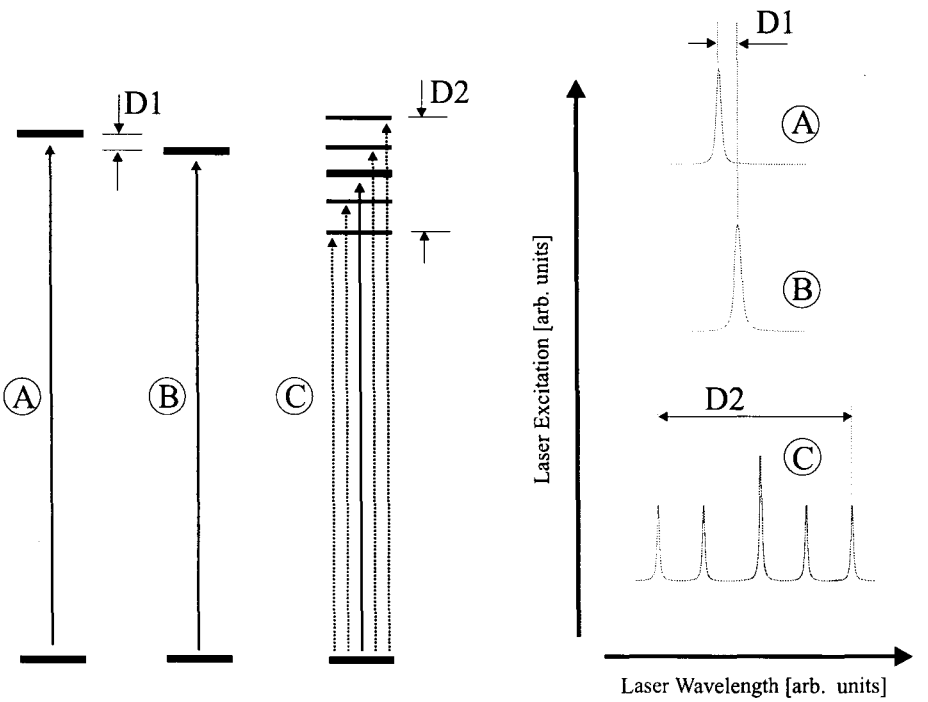

Fig. 3.1: Principle of Stark spectroscopy. On the left side energy diagram with transitions indicated as arrows is plotted for three environments. Straight arrows represent allowed transition. Dashed arrows are the "forbidden" transitions. (A) No electric field. (B) Small electric field. (C) Large electric field. On the right side of the figure the excitation spectra are plotted when the laser scans the transition for the three environments.

Stark spectroscopy methods measure the energy levels influenced by the Stark effect and relate the relative change in the position of transitions to electric field strength and direction by scanning a laser over a transition and measuring the excitation. The relative change in position of the energy level can

be determined. Detecting the event of excitation can be done in several ways and will be discussed in the next chapter. When an typical Stark spectroscopy experiment is done, three kinds of spectra can be measured (Fig. 3.1). In the case of no electric field, the transition occurs at the exact position expected (Spectrum A). In the case of small fields, the position of the observed transition shifts (spectrum B). When energy levels are more closely spaced and the electric field is large, more components can be observed in the spectrum (spectrum C). These observable effects can be directly related to the presence of electric field. The energy ranges $D1$ and $D2$ can be used to identify the electric field strength present in the environment of the atom by comparing them to experimentally or theoretically obtained calibration spectra.

3.2 Stark Effect Calculations

To relate Stark effects to electric field strength or direction, observed spectra need to be either calculated theoretically or be obtained by experiment with known electric field. Theoretically calculating the Stark effects is difficult. In cases where the considered atom is hydrogen-like, theory is available and in this section the method to calculate the theoretical spectra will be described.

To calculate the atomic energy levels the time-independent Schödinger equation for electrons needs to be solved:

$$H\psi = E\psi \tag{3.1}$$

Where H is the hamiltonian of the system, ψ the electron wave functions and E the corresponding energy levels. In this case where electric field is present the hamiltonian of the system is written as:

$$H = H + H_{Stark} = H + eFz \tag{3.2}$$

Where H is the unperturbed hamiltonian and $H_{Stark} = eFz$ the dipole interaction with the electric field. e is the elementary charge, z the direction parallel to the electric field and F the electric field strength. Equation (3.1) needs to be solved and this is in general not possible analytically. To be able to solve Equation (3.1) analytically the potential in the unperturbed hamiltonian $H = -\frac{\hbar^2}{2m_e}\Delta^2 + V(\vec{r})$ needs to be separable.

Laser based Stark spectroscopy uses highly excited levels in atoms called Rydberg states because the influence of the electric field is much larger than with closely bounded states. For the calculation of Stark effects in Xenon or Argon this is an advantage. Rydberg energy levels can be described by the Rydberg hydrogen formula:

$$E_n = \frac{E_{ion}}{(n-\delta)^2} \tag{3.3}$$

E_n is the energy of level with principal quantum number n for quantum defect δ of Rydberg series with ionization energy E_{ion}. For each degenerate level l of principal quantum number n there is a quantum defect δ, and hence a different Rydberg series. In literature the values of the quantum defects for the ns, nd and nf Rydberg series for xenon and argon can be (partially) found [31]-[37]. Quantum defects for $l \geq 3$ are very close to zero, specifying these levels as hydrogen like. For hydrogen like atoms the potential $V(\vec{r})$ in the hamiltonian is coulombic, and Equation (3.1) becomes separable and solvable. Mathematically Equation (3.1) can now be expressed in matrix form. On the diagonal of matrix $H_0 + eFz$ the unperturbed energy levels are placed. The dipole interaction with the electric field will be expressed in the off diagonal elements of the matrix. By diagonalizing matrix $H_0 + eFz$ Equation (3.1) can be solved and the perturbed wave functions with corresponding energies are found.

Before results are presented of this calculation method the elements of the hamiltonian matrix are discussed in more detail. For the case of xenon and argon the Rydberg states can be described by the

jK coupling scheme. There is a strong coupling between orbital quantum l of the Rydberg electron and the total angular momentum of the ion-core j_c. This coupling is described by the angular momentum $K = j_c + l$. The total angular momentum of the atom is then described by $J = K \pm s$, where s is the spin of the Rydberg electron. The energy levels are therefore denoted as $nl[K]_J$, where n is the principal quantum number. The unperturbed wave functions are denoted as:

$$\psi = |nl[K]_J\rangle \tag{3.4}$$

The off diagonal elements describing the interaction can be calculated by integral:

$$\begin{aligned}\langle (nlj_c)KsJM|z|(n'l'j_c)K'sJ'M'\rangle = (-1)^{J+J'+K+K'+l+j_c+s-M}[(2J+1)(2J'+1)(2K+1)\\ \times(2K'+1)]^{1/2}\delta_{MM'}\begin{pmatrix} J & 1 & J' \\ -M & 0 & M \end{pmatrix}\begin{Bmatrix} K & J & s \\ J' & K' & 1 \end{Bmatrix}\\ \times\begin{Bmatrix} l & K & j_c \\ K' & l' & 1 \end{Bmatrix}\langle nl\|r\|n'l'\rangle\end{aligned} \tag{3.5}$$

This integral will only give a result when the two wave functions in question are connected by the selection rules for dipole transitions. In this case for jK coupling:

$$\Delta J = \pm 1 \text{ for } M = 0,\ \Delta J = 0, \pm 1 \text{ for } M \neq 0,\ \Delta K = 0, \pm 1,\ \Delta l = \pm 1,\ \Delta j_c = 0 \tag{3.6}$$

In Equation (3.5) the part containing the $\begin{pmatrix} j_1 & j & j_2 \\ m_1 & m & m_2 \end{pmatrix}$ $3j$ symbol and $\begin{Bmatrix} j_1 & j_2 & j_3 \\ l_1 & l_2 & l_3 \end{Bmatrix}$ the $6j$ symbol express the transition rules. The Kröneckerdelta $\delta_{MM'}$ includes only interaction with $\Delta M = 0$. The last part of the equation is $\langle nl\|r\|n'l'\rangle$ the reduced matrix element:

$$\langle nl\|r\|n'l'\rangle = \begin{cases} -(l+1)^{1/2}\langle nl|r|n', l+1\rangle, & l' = l+1 \\ l^{1/2}\langle nl|r|n', l-1\rangle, & l' = l-1 \end{cases} \tag{3.7}$$

The integral $\langle n, l+1|r|nl\rangle$ can be found in tables of Ref. [23] or be approximated by the hydrogenic formula:

$$\langle n, l+1|r|nl\rangle = (3n/2)[n^2 - (l+1)^2]^{1/2}a_0 \tag{3.8}$$

The Bohr radius is represented by a_0 and this approximation holds for $l \geq 3$. With the above equations the hamiltonian can be constructed. To include all the interactions between all the levels the matrix has to be very large. Fortunately the Stark dipole interaction becomes rapidly weaker for large energy separations. Therefore to calculate the Stark effects a subset of the total levels can be considered reducing the size of the matrix.

When the matrix is diagonalized a new basis set of wave functions is found with corresponding energy levels. The wave functions are expressed as:

$$\psi_\mu^{(n,M)}(F) = \sum_{l=3}^{n-1}\sum_{K,J} Q_{\mu,lKJ}^{(n,M)}(F)|nl[K]_J, M\rangle \tag{3.9}$$

The dimension of the matrix under consideration is expressed by μ. The solutions obtained are according to Equation (3.9) mixed states of the original set of basis functions. The coëfficients $Q_{\mu,lKJ}^{(n,M)}$ represent the amount of mixing. When the atom in the external field is excited from ψ_b, it is now possible to calculated the intensity of the excitation:

$$I_\mu(F) = P_L \sum_{M=-2}^{+2} |\langle \psi_b, M|z|\psi_\mu^{n,M}(F)\rangle|^2 \tag{3.10}$$

3.3 Stark Effect Calculations for Xenon

In chapter four the experimental details of the laser schemes will be described but in xenon it is possible to excite nf states from a metastable state or nd states via 2+1 photon excitation from the ground state. To be able to relate the excitation spectra to electric field the Stark effects for the nf and nd states will be calculated. In order to do so two general assumptions have to be made.

- The calculation procedure assumes the energy levels can be described by the j-K coupling scheme.
- For the $s-, p-$, and d-levels ($l \leq 2$) many levels have been directly measured, and accurately known quantum defects can be used to calculate the energies of unmeadured levels. For the f-levels ($l = 3$) most quantum defects are available from literature, and others can be estimated with reasonable accuracy. For g-levels no information is available. We assume a small non-zero quantum defect, as is the case for argon, and used this to estimate energies. For levels with $l > 4$, energies were estimated assuming a quantum defect of zero.

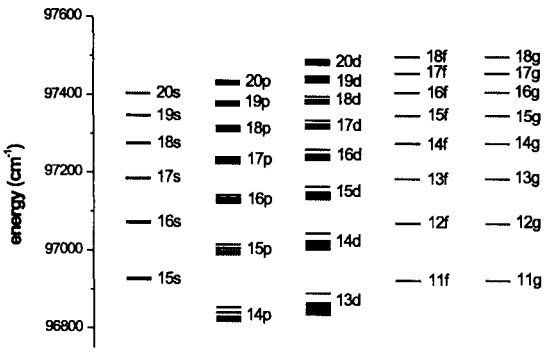

Fig. 3.2: Partial energy level diagram of xenon.

In Figure (3.2) a partial energy diagram is given for xenon. In this diagram can clearly be seen that for high l the levels are very closely spaced as well as for high principal quantum numbers. Also can be seen that for high levels principal quantum number start to overlap resulting in larger matrices to be solved. Hence, to calculate the Stark effects of levels such as 11f, it is necessary only to consider the influence of other n=11 levels with $l \leq 4$ (ie. $11g$, $11h$, ... etc.). Calculation of Stark effects of the $14f$ levels, however, requires consideration of the $17p$, $16d$, $18p$ and $17d$ levels as well as the $14g$, $14h$, ... etc. levels. It is possible to calculate Stark dependence of any of the levels shown in Figure (3.2). Figure (3.3 shows the electric field dependence for two sets of levels. In each case, the theory described in section 3.2 was used to generate these dependences. From the Starkmaps in Figure (3.3) it can clearly be seen that for higher principal quantum number n the complexity increases. The starkmap in the region of $10f$ shows at zero field the separate $10f$ and the degenerate levels $10g, 10h$ until $10(n-1)$. The change of the $10f$ energy levels is quadratic compared to the linear response of the $10g, 10h$ until $10(n-1)$ states

as a function of electric field. This different behavior can be attributed to the fact that levels with $l \geq 3$ have almost zero quantum defects. Stark maps of hydrogen clearly show this linear behavior.

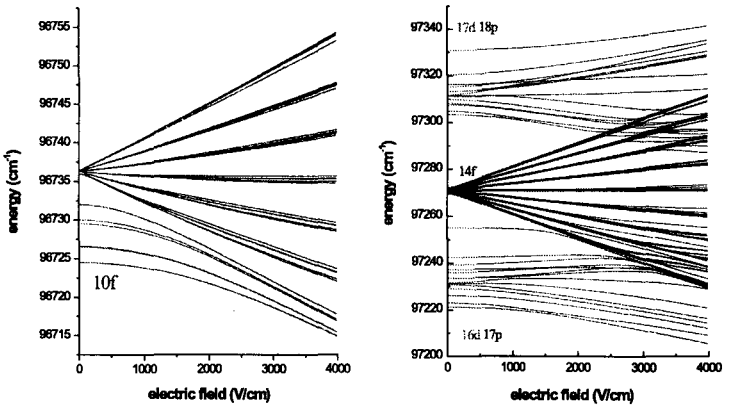

Fig. 3.3: Xenon stark map for the $10f$ and $14f$ region.

Figure (3.3) shows electric field dependence of particular sets of levels, but what is actually measured with stark spectroscopy is an excitation spectrum. Examples of these are shown in Figure (3.4). When a Stark spectroscopy measurement is performed the laser is scanned from 486.4 until 487.6 nm in the region where electric field is measured. Excitation peaks are detected and by comparing the measured excitation spectra with the spectra depicted in Figure (3.4), the electric field magnitude can be determined.

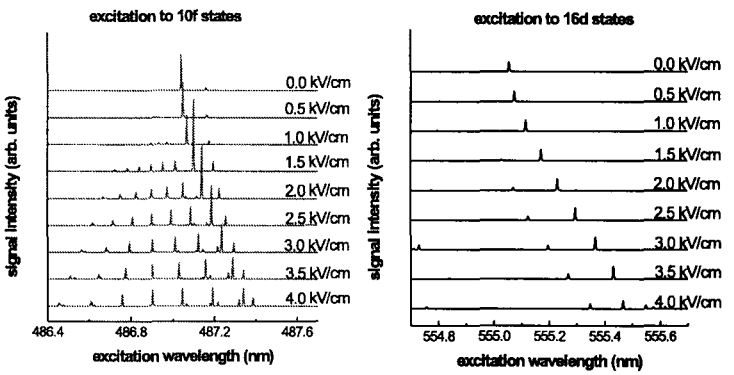

Fig. 3.4: Excitation spectra for excitation to the $10f$ and $16d$.

The way levels respond is determined by the vicinity of optically connected levels. For the $16d$ case this is clearly different to the $10f$ case and the sensitivity of these levels to electric field is also different. Electric field sensitivity can be plotted and this is done in Figure (3.5) by plotting the shift or splitting of observed lines as a function of the electric field.

Sensitivity as a result of the response of the observed lines to electric field show linear and quadratic behavior for respectively nf and nd states. To be able to measure small electric field strength one should therefore choose to use excitation to nf states. For small electric fields this can still give good resolution in comparison with the nd states. In Figure (3.6) the ability of the diagnostic to measure small electric fields is illustrated. The results in Figure (3.6) obtained by the simulation suggest electric fields in the order of 40 V/cm is the minimum resolvable electric field strength. At zero field two excitation peaks

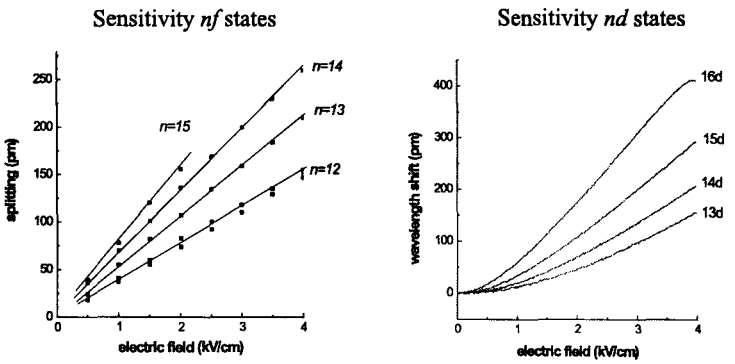

Fig. 3.5: Sensitivity diagrams for excitation to nd and nf states.

can be recorded for excitation to $14f$ similar to those for excitation to $10f$. The Stark components start to appear at 40 V/cm determining the minimum resolution. As can be seen in the sensitivity diagram for f states as well as the Stark maps the maximum resolution is determined if peaks can be assigned. Peaks in the excitation to $16d$ can be easier assigned for high electric fields than for excitation to $14f$.

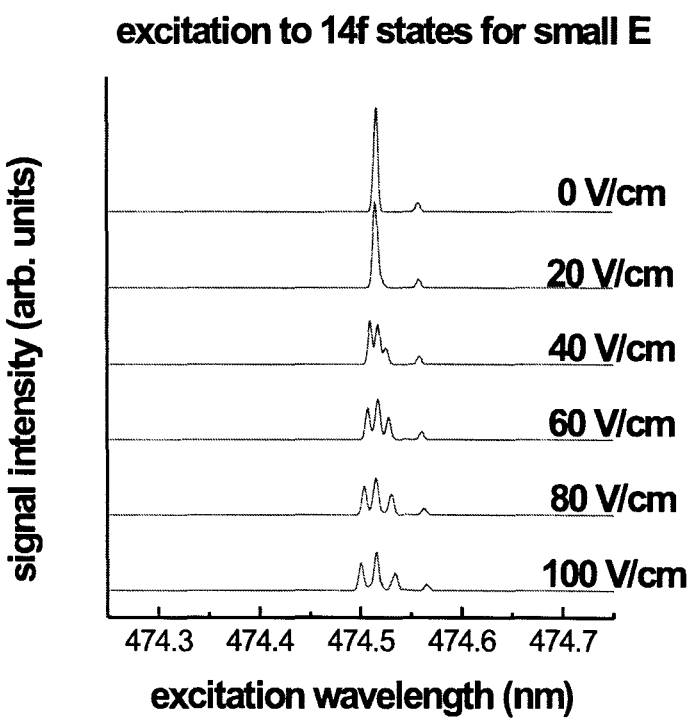

Fig. 3.6: Excitation to $14f$ spectra for small electric fields.

Chapter 4

Experiments

The second feature of the diagnostic development is the validation in experiments. A stable discharge, with well-defined electric fields, namely a negative DC glow discharge will be used. In chapter two the electric field distribution in this kind of discharge is discussed and in this chapter the experiments used to measure these electric fields will be evaluated. The first section describes the experimental schemes, the set-ups to realize these experiments are described in the second section.

4.1 Experimental Schemes

The experimental scheme that will be used to develop and possibly validate the electric field diagnostic are discussed in this section. The first experimental scheme is to determine the electric field in the sheath of a negative DC glow discharge with one photon excitation from a metastable state of xenon. For the development of the micro discharge diagnostic, a second xenon scheme will be considered.

4.1.1 1 Photon Xenon Stark Spectroscopy

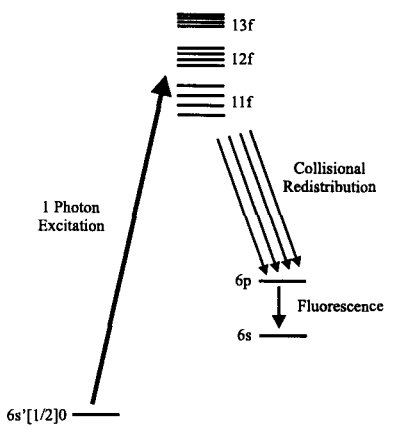

Fig. 4.1: One laser excitation scheme for electric field diagnostics using Xenon.

The first xenon scheme uses one laser ($\pm$ 490 nm) to excite to the Rydberg nf states (see Figure (4.1)) from the the metastable state 6s'$[1/2]_0$. For xenon the 6s' state is a mixture of an 6s' and a 5d state, so excitation to the f states is allowed. Excitation will be determined in a similar way as in the case of argon [15]. For some plasma condition, through collisional redistribution the $6p$ level is populated and this level de-excites to $6s$ by emission of a photon around 823 nm. Two detection techniques can therefore be used to detect the excitation. Either detection of the Laser Opto Galvanic (LOG) signal by

monitoring the voltage over the electrodes or detecting the collisional Laser Induced Fluorescence (cLIF) signal. With the LIF detection method the temporal and spatial resolution of the diagnostic should be respectively in the order of 100 ns and 100 μm. Only the positions in the discharge with enough xenon metastables can be used to validate this scheme. For a DC glow discharge this is not a strict limitation but for the development of a micro discharge diagnostic a second scheme should be considered.

4.1.2 2+1 Photon Xenon Stark Spectroscopy

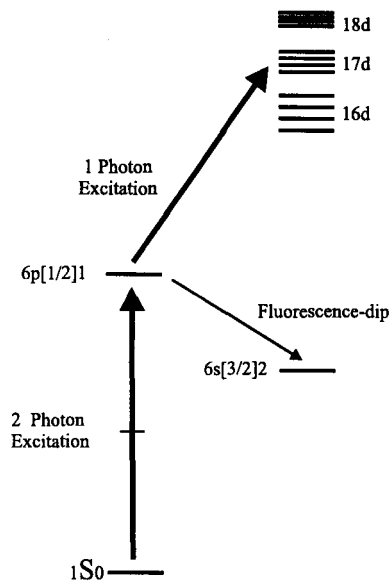

Fig. 4.2: 2+1 Photon scheme for xenon Stark spectroscopy.

For the second scheme (Figure (4.2)) an intermediate $6p[1/2]_0$ is prepared by two photon excitation (2x 249.6nm) from the ground state $^1S_0$. This state relaxes to the $6s[3/2]_1$ state by emitting a 828 nm photon. The LIF is a measure of the increase of population by the two photon excitation from the ground state. Whenever the second laser ($\pm$ 600 nm) excites to a Rydberg state a dip in the LIF will be observed [18], because of the relative decrease in population of the $6p[3/2]_1$ state. Compared with the one photon scheme describe above, this scheme is experimentally difficult to execute. Two lasers need to be aligned in space and time as well as the detection of the diagnostic method. The ability to measure at any time or space in the discharge offers no limitation. Resolution of this method is also expected to be in the order of 100 ns and 100 μm.

4.2 Experimental Set-Up

For all the experiments in this master thesis a general configuration is used (Figure (4.3)). The set-up consist of two laser systems, an excimer pumped and a YAG pumped dye-laser. The lasers are focussed in the discharge cell by optical components. The discharge cell contains a mixture of xenon and argon and two parallel electrodes. Two power supplies are connected in series to create a DC negative voltage between the electrodes. The current through the discharge is limited by a ballast resistor. When the gas breaks down a negative glow discharge is formed above the bottom electrode. Electric fields will be measured in the sheath between the glow and the electrode. The voltage between the electrodes is monitored with a high pass filter which is connected to a Tuedacs data acquisition system. The data acquisition system samples the voltage signal as a function of the time to be analyzed in software later.

Perpendicular to the laser beam, detection optics are placed to observe the LIF signal. A 25 cm monochromator with a 1200 lines/mm grating is placed between the detection optics and a ICCD camera to measure the LIF spectrum. The lasers and ICCD camera and the data acquisition system are synchronized by a delay generator. All the optical paths have optical components for simplicity depicted in Figure (4.3) as O1 ,O2 and O3.

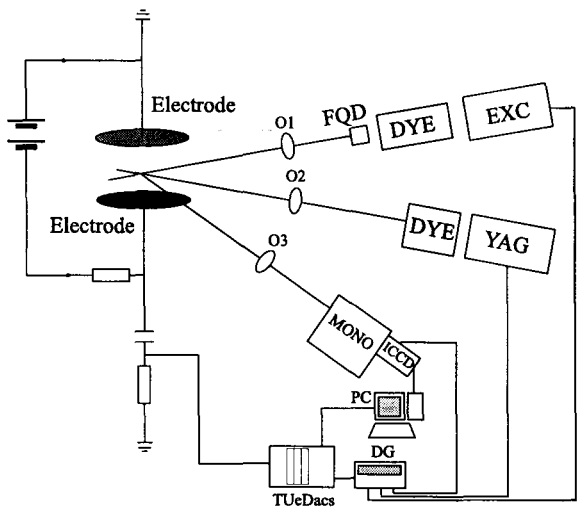

Fig. 4.3: Schematic overview of the experimental arrangement. An excimer pumped dye laser (EXC), monochromator (MONO) plus ICCD camera, delay generator (DG), personal computer (PC), electrode configuration and a TUeDacs data acquisition system. There are several components in the optical paths (O1, O2 and O3).

4.2.1 Discharge

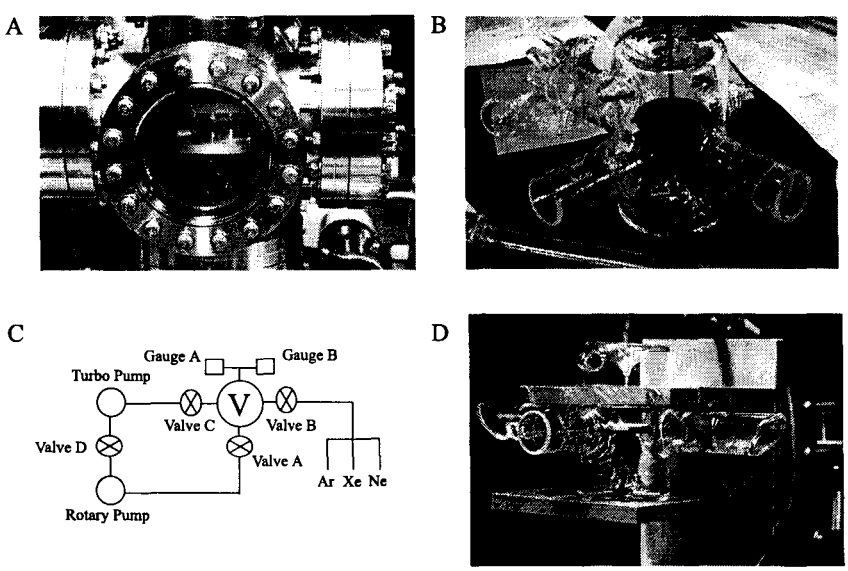

Fig. 4.4: (A) Picture of the electrode configuration in the vacuum chamber. (B) First test tube arrangement. (C) Schematic overview of the vacuum system. (D) The second test tube arrangement.

Two systems were designed, a glass test tube and a vacuum system with two electrodes. Both systems are illustrated in Figure (4.4). The discharge tube (4.4B+D) has three quartz windows, two electrodes and

a gas mixture containing xenon and argon. The second system, which was designed for microdischarge measurements, is shown in Figure (4.4A+C). For testing of the electric field diagnostic an electrode configuration is inserted in the vacuum system. The electrode configuration can be translated in height by a manipulator.

A schematic overview of the vacuum system is given in Figure (4.4C). On the vacuum system there are two gauges, a gas inlet, connection to a turbo pump and a rotary pump. There is a bypass connection between the turbo and rotary pump. Three different gas species are connected, xenon, argon and neon. By closing valve A, B and C the vacuum vessel can be closed. All components of the vacuum system are from RVS material and the vacuum connections are copper caskets, to allow a good vacuum ($\approx 10^{-6}$ mbar) and very small introduction of impurities while the system is closed (< 0.1 mbar/h).

4.2.2 Excimer Pumped Dye-Laser

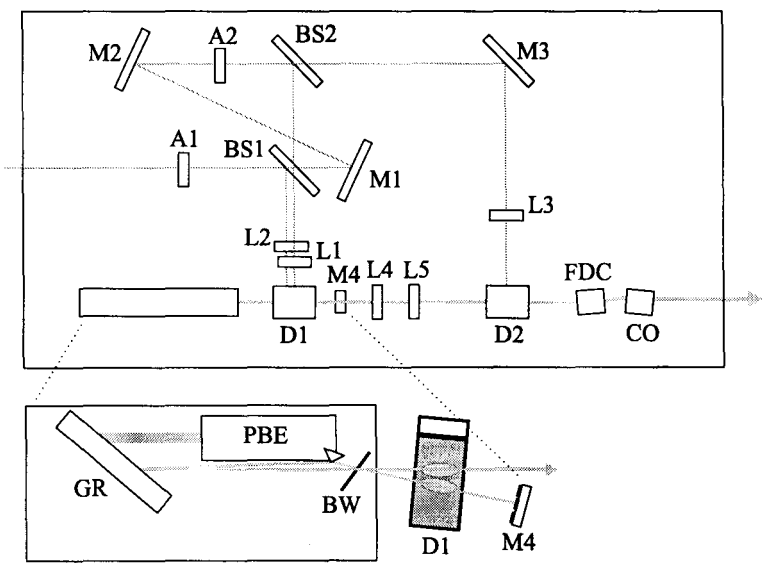

Fig. 4.5: Schematic outline of the optical components inside the dye laser. There are attenuators (A1, A2), beamsplitters (BS1, BS2), mirrors (M1 until M4) and lenses (L1 until L5). The pump beam passes through two dye cells (D1 and D2). There is a frequency doubling crystal (FDC) and compensator (CO). Futhermore there is the grating (GR), a prism beam expander (PDE) and a Brewster window (BW).

The tunable laser used is an excimer pumped dye laser. The excimer laser (Lambda Physik) pumps the dye laser (Lambda Physik FL3002) with 308 nm photons. It is a pulsed laser with an approximate pulse length of 30 ns. The configuration of the dye laser is depicted in Figure (4.5). The pump beam enters the system on the left and can be attenuated. It passes through a beamsplitter splitting the beam into two parts. The reflected beam is focussed in the dye cell and the beam which passes through the beamsplitter goes via mirrors and an attenuator to the second beamsplitter. Again the beam is split up in two beams, one is focussed in the first dye cell, the other is focussed into the second dye cell. The laser cavity is enlarged in the bottom section of Figure (4.5). The first dye cell acts as an oscillator and a pre-amplifier. Two ellipses indicate the pump beams passing through. The dye is excited and gives fluorescence within a certain range determined by the properties of the dye molecule. Only the wavelength reflecting from the grating will start the oscillation which leads to the laser effect. Part of this laser beam is split of unto the grating and reflected back in the dye cell to be pre-amplified. The Brewster window ensures there are no reflections of the beam passing through. The exact wavelength is determined by the angle of the grating. To increase the wavelength resolution a prism beam expander is used to use a larger area of the grating. The laser beam is expanded by two lenses before it enters the

second dye cell. A 3 mm beam will enter the second dye cell and the intensity is amplified by a factor of 20. If desired the laser beam can be frequency doubled by a frequency doubling crystal (this done to generate UV light). This crystal alters the beam path slightly and this is compensated by a compensator crystal. The laser beam leaves the dye-laser on the right hand side.

4.2.3 Laser Dyes

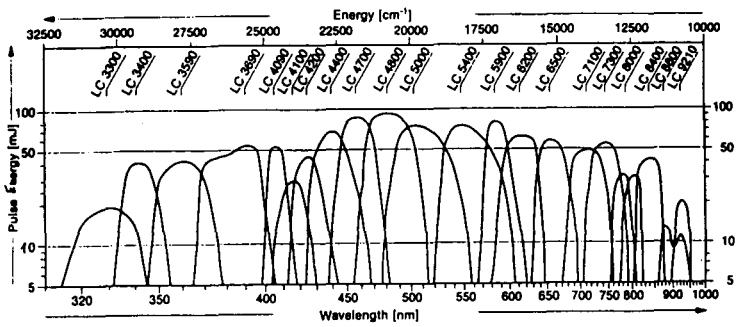

Fig. 4.6: Dye-tuning curves for excimer pumped dye-laser.

The dye-laser uses dye solutions to generated the specific wavelength. The main advantage of this method is the possibility to tune the laser wavelength. This is in both dye-lasers done by changing the angle of the grating. The wavelength range for each dye is rather limited, the energy conversion and life time are also not always very good. Figure (4.6) shows some of these dyes and their tuning curve. For the schemes mentioned previously in this chapter different dye-solutions are needed. The first xenon scheme uses a dye, generating laser light around 480 nm. The second scheme needs two lasers with each having a different dye, to generate 500 nm (frequency doubled to 250 nm) and 560 nm beams. The dye is circulated through the dye cells and to be able to use all these different dye solutions two dye circulator systems are used. Changing dyes will in general give problems when going from a higher to a lower wavelength, because these dyes do not mix well together and decrease the performance of the laser substantially when mixed.

4.2.4 Triggering and Acquisition

Synchronization of all the measurement systems is essential for this measurement. A delay generator with picosecond time resolution is used to synchronize the acquisition. In Figure (4.7) the timing schedule is depicted for a two laser experiment. The 2+1 photon scheme would require this kind of operation. In this case the second laser is a YAG pumped dye-laser. For the YAG laser to fire two trigger signals are needed. The first signal triggers the lasers flashlamps at 30 Hz. This signal can either be generated by the delay generator or by an external function generator. The delay generator triggers from the positive slope of this 30 Hz signal at moment T_0. The delays needed for synchronization are set from T_0. A pulse of laser light is generated at the moment a trigger arrives at the Q-switch and after the time needed for the laser pulse to travel from the laser to the discharge the camera needs to be triggered. The excimer laser needs one trigger to be fired, but the time between the trigger is in the order of microseconds, requiring triggering of the excimer before the Q-switch of the YAG laser. For the detection of the LIF signals the camera is needs to be gated by feeding a pulse to the gater of the camera. Such a pulse can also be generated by the delay generator.

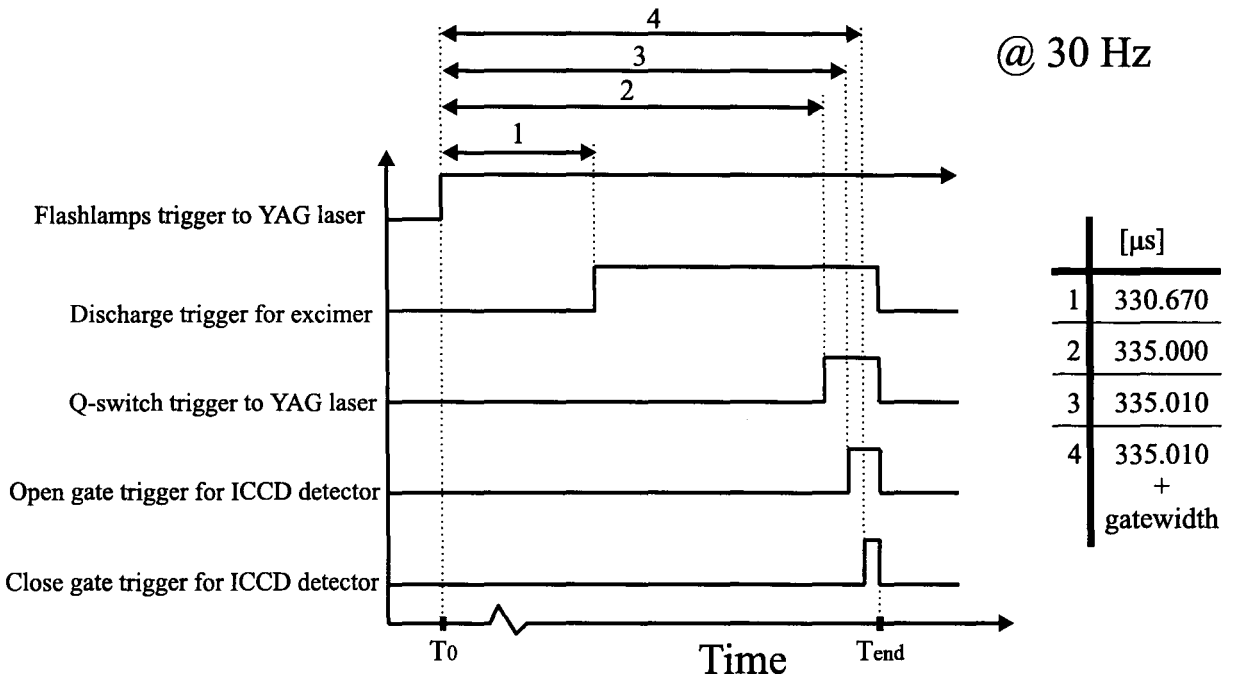

Fig. 4.7: Timing schedule for the triggering of a two laser experiment.

4.2.5 ICCD Camera

For the detection of the LIF signals an Andor ICCD camera is used. This camera can be gated with nanosecond resolution. Andor software provides the possibility of operating the camera in different modes. The acquisition can be set to take a LIF signal every laser wavelength step as well as averaging a typical amount of shots per wavelength step. Data is stored on the computer for analysis later. In Figure (4.8) the schematic overview is given for the camera. The trigger for the gating arrives at the gate input, which is transferred by the gating electronics to the image intensifier. Through the photocathode and the fiber optic coupler photons will reach the CCD chip. The CCD chip is cooled by a three stage cooler, water and air assisted cooling to reduce dark currents. Control of the shutter and data transfer between the camera and the computer is dealt with by the electronics in the back of the camera. Two possible configurations are possible for triggering the camera. Either to trigger the laser or receive a trigger from the laser. For all the experiments presented in this thesis the laser was triggered via the delay generator which also triggers the camera.

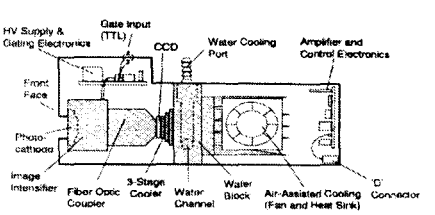

Fig. 4.8: Schematic drawing of the ICCD camera.

4.2.6 LOG Circuit

In order to monitor the impedance of the discharge a LOG circuit is designed [25]. This circuit measures the voltage across the discharge with a high-pass filter. The circuit is designed to be connected to the TueDacs data acquisition system which allows only input voltages between -1 and +1 Volt. An operational amplifier is used as a buffer for this data acquisition system. The diodes on the positive side of the amplifier limit the voltage to two times 0.6 Volts positive and negative. The TueDacs system samples the voltage as a function of time and stores it in the computer's memory. The TueDacs system also requires a trigger which is taken from the delay generator.

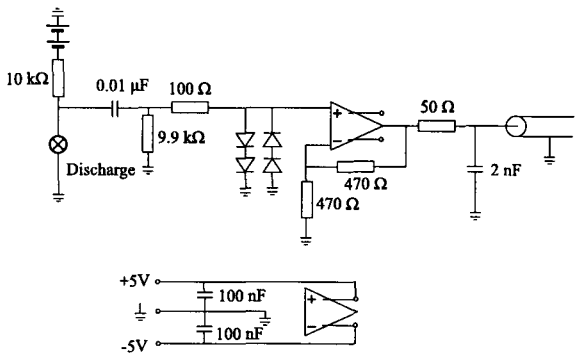

Fig. 4.9: Schematic drawing of the circuit used to obtain the Laser Opto-Galvanic (LOG) signals.

Chapter 5

Experimental Results and Conclusions

The theory used to calculate Stark spectra is explained in chapter three. The experimental schemes described in the previous chapter will be used to detect these transitions in the sheath of a negative DC glow discharge. By comparing the transitions to theory the electric field strength will be determined. How transitions are observed by the LOG detection method is described in the first section. In the second section the experimental condition will be outlined, the obtained Stark spectra will be shown in the third section.

5.1 LOG Spectroscopy

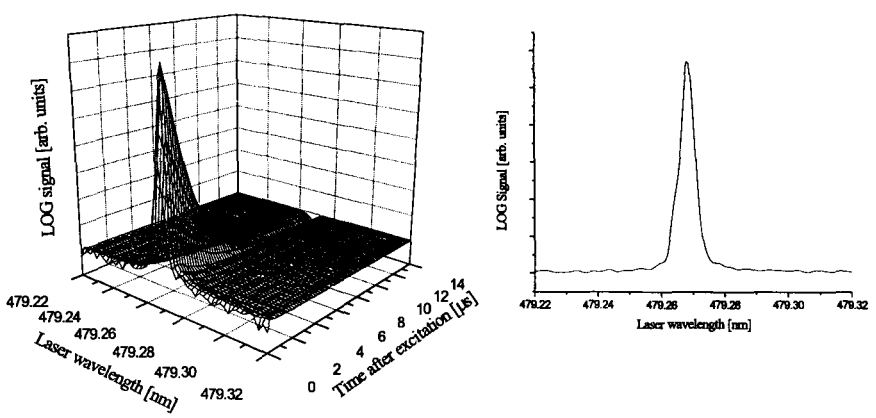

Fig. 5.1: On the left side a three dimensional plot of the LOG signal while scanning the laser wavelength over the $6s[3/2]_2$ to $7p[1/2]_1$ transition. The front axis shows the laser wavelength, the side axis the time after excitation and the vertical axis the measured voltage. On the right the resulting excitation spectrum is plotted.

For a LOG experiment, the impedance of the discharge is monitored during a wavelength scan of the laser. Figure (5.1) shows the results of a LOG experiment in which the strong xenon $6s[3/2]_2$ to $7p[1/2]_1$ transition was observed. The dependence of the LOG signal on wavelength and time is plotted. In this case, the laser was scanned from 479.22 nm to 479.32 nm with steps of 2 pm. At each wavelength, the signal from 50 laser shots was averaged. Excitation by the laser is indicated by the increase in the LOG signal, which rises very rapidly and then falls away over a time period of several microseconds. In this case by averaging the voltage measured between 1 and 2 μs after laser presence an excitation spectrum

corresponding to the $6s[3/2]_2$ to $7p[1/2]_1$ transition can be determined (Figure (5.1))

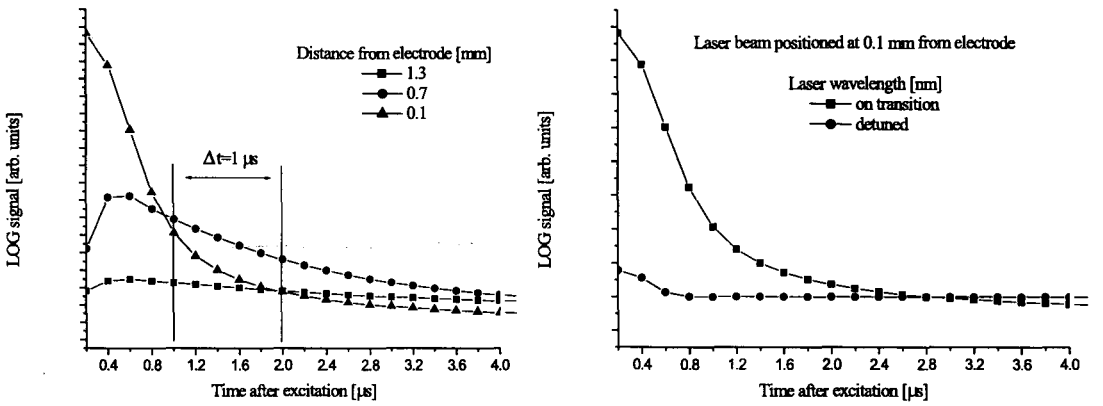

Fig. 5.2: The definition of the distance from the electrode at the top. The left graph shows the LOG signal as a function of the time after excitation from to $6s[3/2]_2$ to $7p[1/2]_1$ for three different distances from the electrode. The right graph shows the LOG signal as a function of time after excitation for two laser wavelengths.

The response of the LOG circuit is dependent on the position of the beam in the discharge. This effect is illustrated in Figure (5.2) by plotting several LOG signals as a function of the time after excitation. In the left graph, three LOG signals for different positions of the laser beam are plotted as a function of the time after excitation, with the laser wavelength at the $6s[3/2]_2$ to $7p[1/2]_1$ transition. When the beam is positioned 1.3 mm from the cathode the signal is relatively small compared to the signal at 0.1 mm and the response is slower. The time frame in this graph gives the period which is considered for averaging. This is related to the graph in the right side of Figure (5.2). If the laser, at a position close to the electrode, is detuned from the transition wavelength a significant background signal is observed. The reflections, which are a result of the laser beam passing through optical components, induce stray light hitting the electrode. The response of the LOG circuit to this effect is similar to a response to a transition but much faster. Because this was always observed in the first 0.8 μs after excitation, LOG signals corresponding only to excitation in the plasma can be observed at times after 0.8 μs.

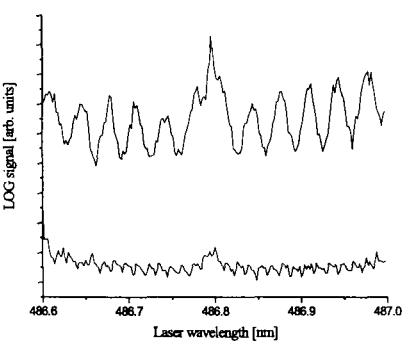

Fig. 5.3: LOG spectra taken with laser beam passing through the flat windows (top) and not passing through the windows (bottom).

The background LOG signals are also dependent on laser intensity. In Figure (5.3) oscillation are observed in the excitation spectra. These spectra where taken from the discharge tube (Figure (4.4B))

through the windows and the side of the tube. The modulation is clearly obscuring the spectra to be observed.

5.2 Experimental Conditions

In Figure (4.3) the set-up is outlined. For the measurements presented in the rest of this chapter only the excimer-dye laser is used. For the first experiments the discharge tube was used (Figure (4.4D)) with a mixture of 10% xenon and 90% argon at a pressure of 10 mbar. The main problem experienced with the discharge tube is illustrated in Figure (5.4).

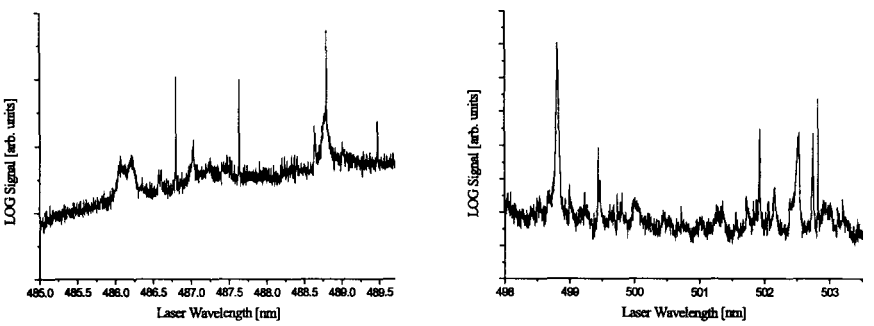

Fig. 5.4: Excitation spectra for a wide range taken from the discharge tube.

Peaks unrelated to transitions of xenon or argon are observed. The main cause for this is the several dirty spots on the electrode, which could be observed visually. Peaks can not be clearly discriminated from this background and therefore the more flexible configuration of the vacuum system was used for further measurements.

To test the one photon scheme of xenon, explained in the previous chapter, LOG signals were taken for transition ranges predicted by the calculation in chapter three. The excimer-dye laser was scanned 2 pm per wavelength step and the LOG spectra of one wavelength step contained an average of 50 laser shots. In software the excitation spectra were obtained by averaging the LOG signals between 1 and 2 μs after laser presence and plotting this averaged LOG signal as a function of the laser wavelength. The laser was operated at roughly 1 mJ/puls and the laser beam was focussed in the vacuum chamber by a cylindrical lens with a focal length of 300 mm. The voltage put across the electrodes plus ballast resistor was 300 Volts. Because of the unstable behavior of a pure xenon discharge, a gas mixture of 40% xenon with 60% argon at a pressure of 20 mbar was chosen. The laser beam passed through the discharge 0.4 mm from the electrode, parallel to the electrode configuration.

5.3 Experimental Results

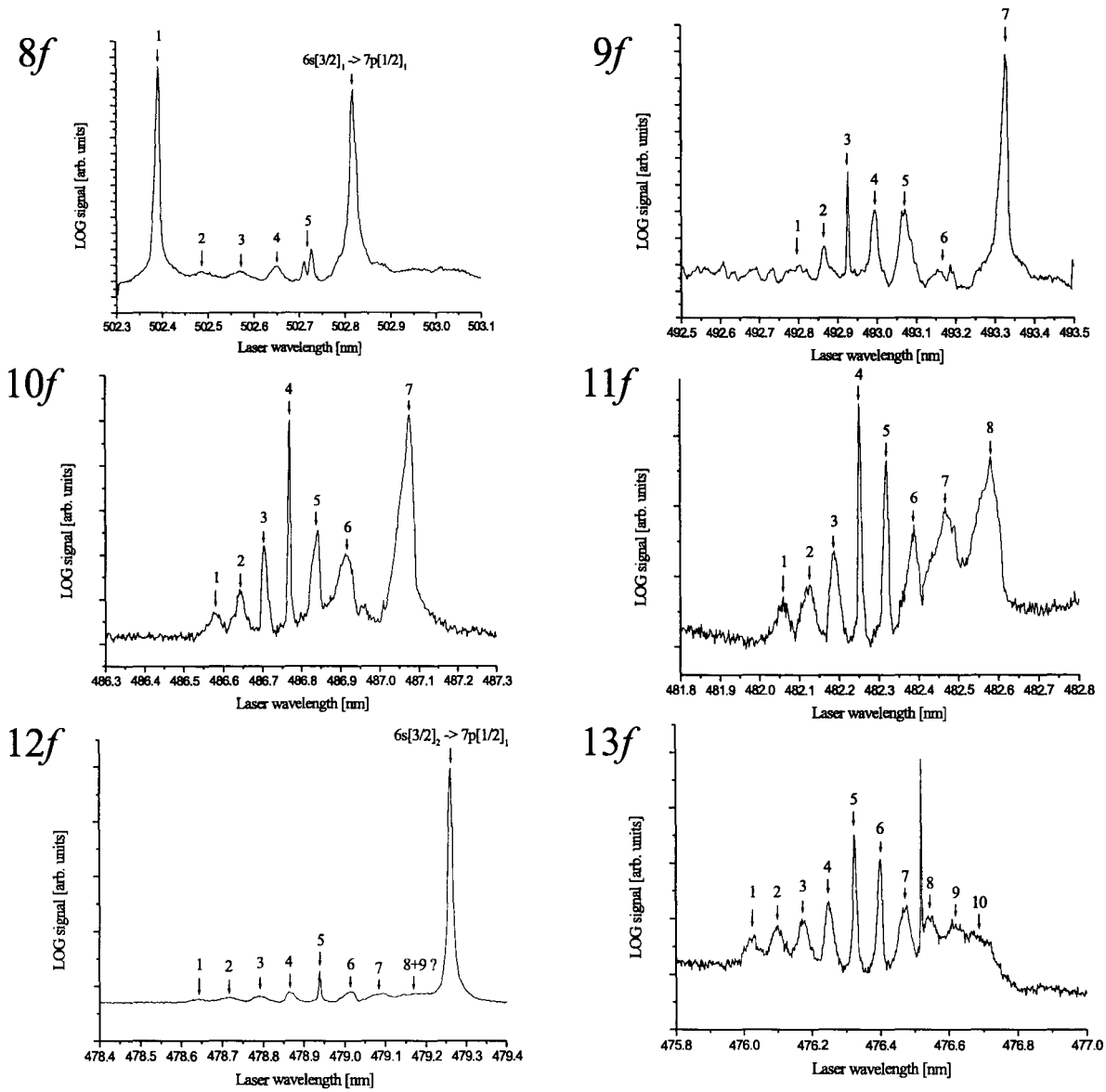

Fig. 5.5: Observed LOG spectra for $8, 9, 10, 11, 12$ and $13f$ excitation from $6s'[1/2]_0$.

Collisional induced laser fluorescence was not found for these experimental conditions. Therefore in Figure (5.5) the observed LOG excitation spectra are plotted for wavelength regions where $8, 9, 10, 11, 12$ and $13f$ excitation can be expected. Several features can be noted of the spectra.

- Peaks are observed in the excitation spectra not related to the Stark effect. LOG spectroscopy detects all excitations, so e.g. also the $6s[3/2]_2 - > 7p[1/2]_1$ transition appearing in the $12f$ spectrum. This can partially obscure the Stark spectra.

- The spectra obtained for 9 until $13f$ have Stark-like structure. For the $8f$ level no Stark components could be determined, although the transition $6s'[1/2]_0 \rightarrow 8f[3/2]_1$ could be identified.

- Number of peaks observed as a function of the principal quantum number n increases, as expected.

Changing the experimental conditions should influence the spectra. By taking measurement at different positions in the sheath should result in difference in spectra. For the $13f$ excitation two positions were taken and are plotted in Figure (5.6). The spectrum at 0.4 mm should represent a substantial larger electric field then at 1.2 mm. This can be seen by the fact the manifold is smaller in width. At 1.2 mm distance from the electrode the electric field is almost zero and no Stark splitting is expected. However Stark splitting is still observed, and this could imply poor spatial resolution or part of the beam passing through a region with electric field.

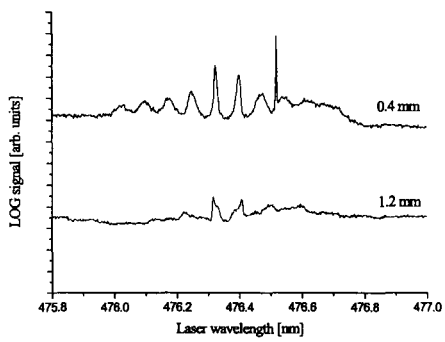

Fig. 5.6: Transition region of $13f$ for two different position, 0.4 and 1.2 mm from the electrode.

The pressure of the discharge also effects the electric field distribution. When the pressure is decreased, the sheath width increases. This results in a lower electric field at the same spatial position. The pressure of the discharge was 20 mbar when the pressure is decreased Figure (5.7) shows three spectra taken for different pressures at the same spatial position. The same behavior as by changing the spatial position is found by changing the pressure. The only feature in the spectrum which does not move and only decreases in intensity is the sharp peak beween peak 7 and 8. Therefore it can be concluded that this feature is not related to the Stark spectrum. The decreasing size of the manifold is in this case much clearer and for three different electric field strengths, spectra can be measured.

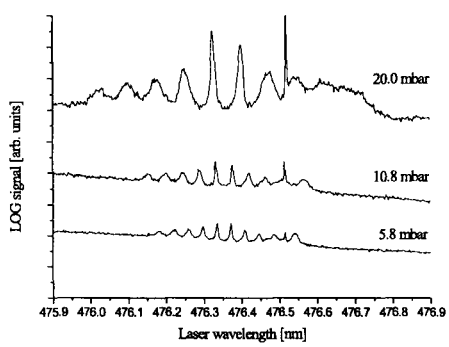

Fig. 5.7: Transition region of $13f$ for different gas pressures, 5.8, 10.8 and 20 mbar .

It can be concluded that the observed spectra are Stark spectra. Detailed comparison of the spectra with theory will be presented in the next section, but even examining just general features, we conclude that we are observing spectra influenced by the electric field inside the discharge.

5.4 Comparison with Theoretical Calculation

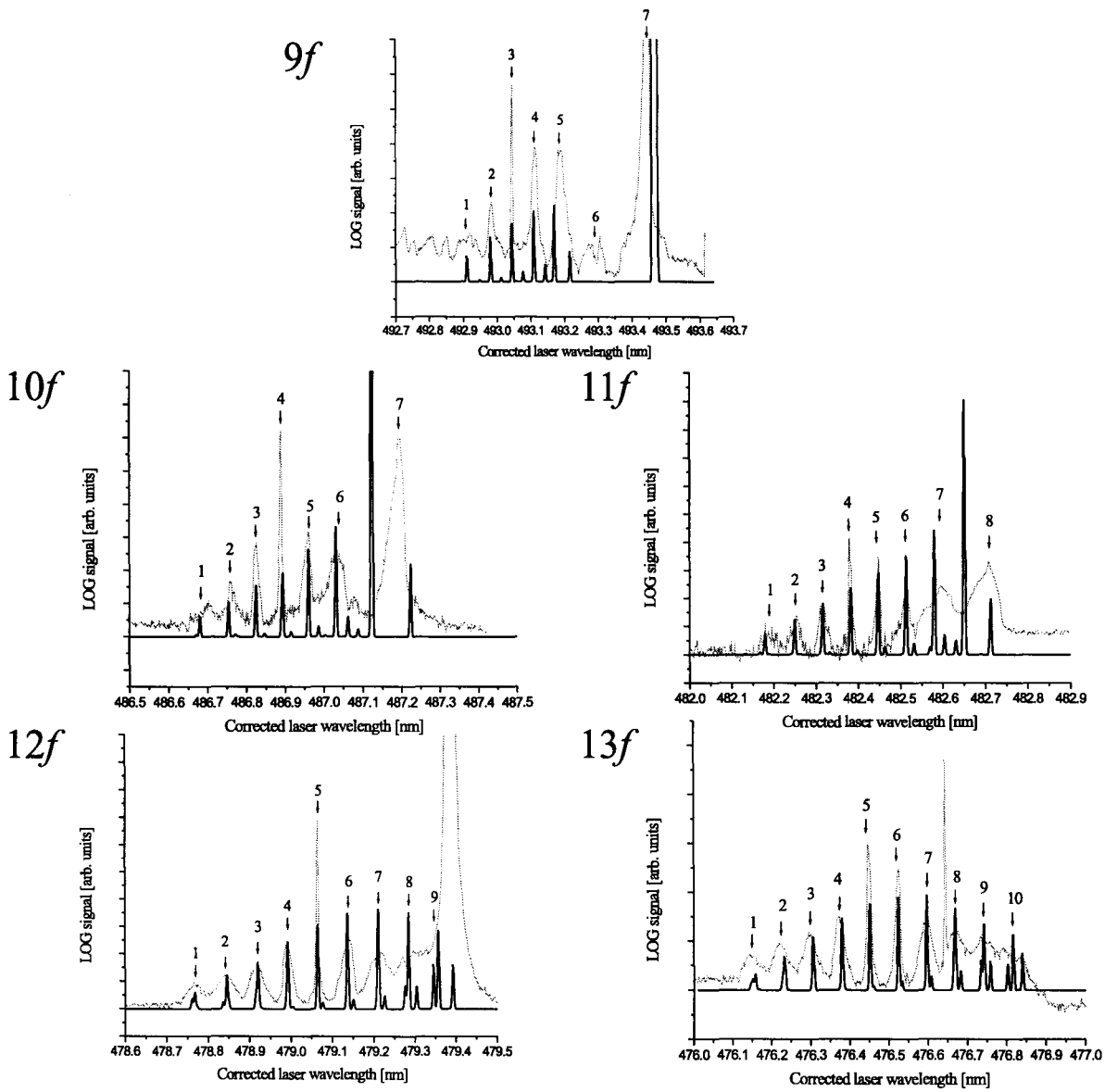

Fig. 5.8: Experimental LOG spectra compared with calculated spectra for $9, 10, 11, 12$ and $13f$ excitation from $6s'[1/2]_0$.

In Figure (5.8) the obtained spectra from the previous section are compared to those calculated by theory of chapter three. Determining the electric field strength by comparing calculated to experimental spectra results in a electric field strength of (1800 $\pm$ 50) V/cm at 0.4 mm from the electrode. This electric field strength is determined by the spacing of the Stark components. In each case, the wavelength case of the experimental data has been shifted to match the calculated data. In Table (5.1) the determined electric field strengths are tabulated for each individual spectra as well as the shifts. The shifts of the data has no influence on the electric field strength of 1800 V/cm, but gives an indication of the accuracy of the calculation in determining as well as the laser reproducing the absolute wavelengths of the transitions. Some features of the comparison between experimental and theoretical data can be noted.

- There is excellent agreement for large n and somewhat poorer agreement for small n. For example, peak 7 in the spectrum of $9f$ cannot be fitted by theory, but the positions of all the peaks in the observed $13f$ spectrum are predicted well in the calculated spectrum.
- The calculated relative intensity distribution is different for most spectra but also for larger n better agreements is found.
- The outer peaks are wider than the central peaks. This can be explained to be a result of the gradient of electric field within the volume of the laser beam. The outer transitions are more sensitive to electric field than the central transitions (e.g. $13f$ spectrum in Figure (5.8)), and so the gradient in electric field affects the outer peaks more than the central ones.
- The spectrum e.g. of $13f$ shows more complexity on the right side then on the left. This is due to the mixing of the f-states with the $g, h, ...etc.$-states. This also very well observed in the theoretical and experimental spectra.

Table 5.1: Electric field strength by comparison of calculation with experimental spectra.

f-state	E-Field Strength [V/cm]	Shift [pm]
8	-	-
9	1750 ±50	118.0
10	1850 ±50	120.0
11	1750 ±50	127.5
12	1800 ±25	125.0
13	1800 ±25	125.0

To show how the electric field diagnostic can be used the spectra in Figure (5.7) were matched with theoretical spectra and the electric field was determined. This is illustrated in Figure (5.9).

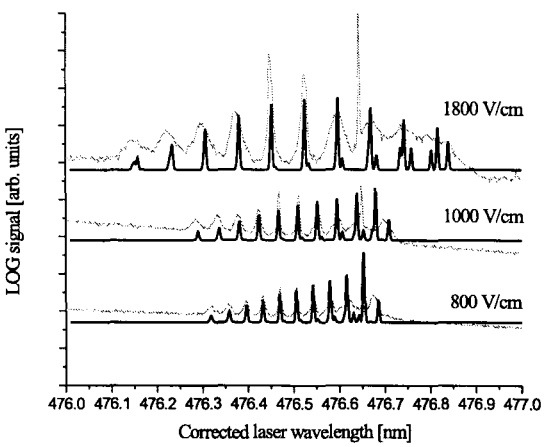

Fig. 5.9: Transition region of $13f$ for different gas pressures at 0.4 mm from the electrode. The experimental data is plotted (gray) as well as the theoretical spectra (black).

It can be concluded that the theory explained in chapter three can accurately predict the Stark spectra in xenon, with better agreement for large n. With these theoretical spectra electric field strength can be determined.

Chapter 6

Discussion

The Stark spectra described in the previous chapter will be discussed in this chapter. In the first section the match of the calculated to the experimental spectra will be discussed. The resolution of electric field measurements will be discussed in the second section.

6.1 Theoretical Calibration

The comparison of experimental data and theoretical spectra in the previous chapter indicated that excellent agreement was found for transitions to higher n, but the agreement was noticeably poorer for smaller n. This trend can be understood by considering some aspects of the theoretical spectra and the way they are calculated.

6.1.1 Zero Field Positions

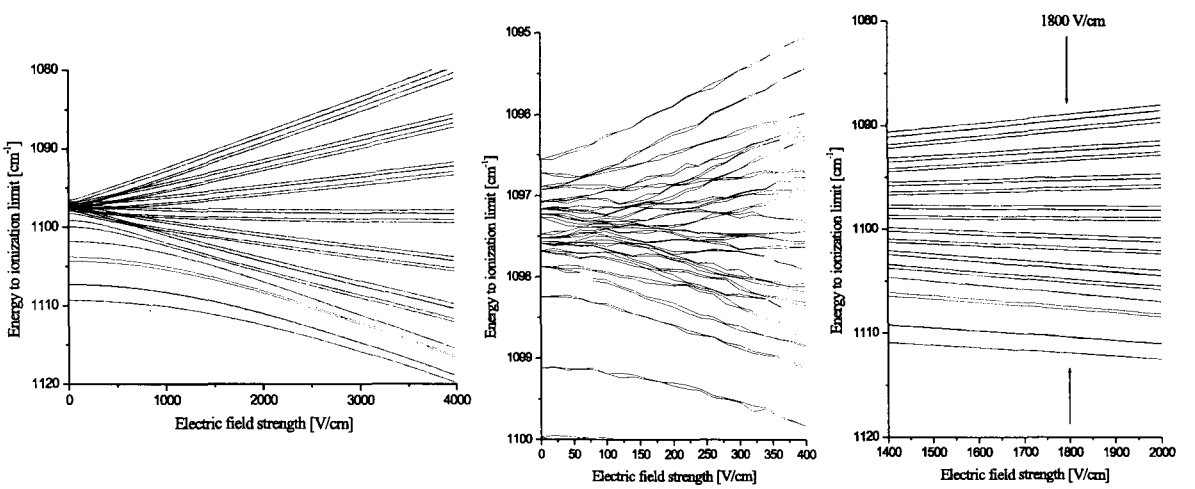

Fig. 6.1: Calculated energy levels as a function of the electric field for the $10f$ states.

The method for calculating theoretical spectra, explained in chapter 3, determines the positions of each energy level by considering the mixing between a large number of energy levels. However, the normal energies of these levels (i.e. when electric field strength is zero) are mostly unknown, and so these zero field energies were estimated. Three assumptions were made for the zero field positions of the xenon energy levels. Quantum defects are considered zero for $l > 4$. The quantum defects of the f-states

are partially known and for the g-states none are known. For the f-states missing quantum defects were extrapolated from known literature values and for the g-states an quantum defect between zero and the ones of f were chosen. Error in the estimation of the zero-field energies would affect the accuracy of the calculation, with the problem being more significant for low n than for higher n.

The influence of the initial positions can be illustrated if the Starkmaps of 10 and $13f$ are compared. In Figure (6.1) the Stark map is plotted for $10f$, which includes all the levels (not only the ones that can be excited from $6s'[1/2]_0$). The left plot shows the splitting of the levels into $n-3=7$ groups at 4000 V/cm. For the case considered in the results at 1800 V/cm the peaks are well separated and the separation is about ten times larger then the separation of the $l>4$ levels at zero field, plotted in the middle.

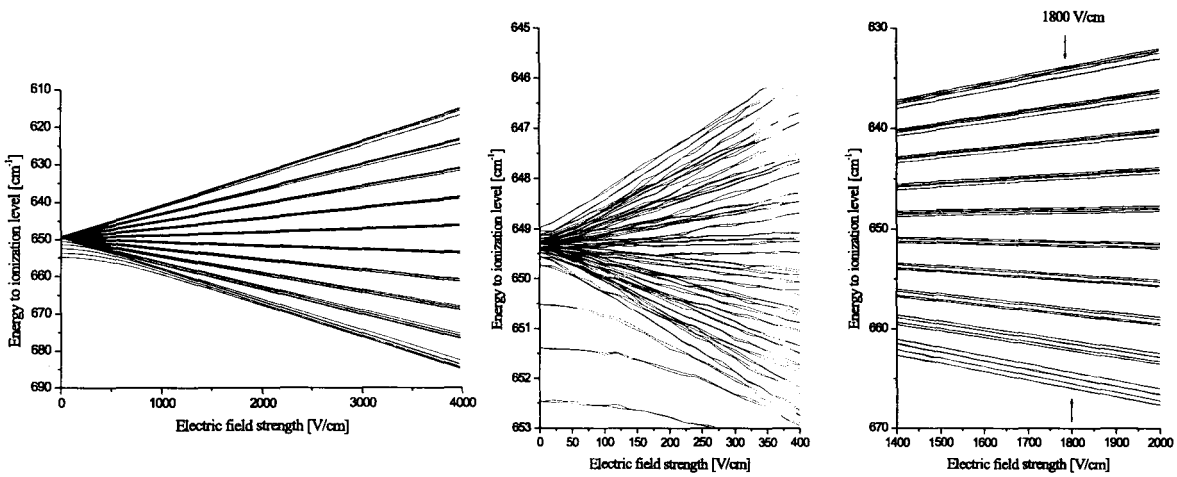

Fig. 6.2: Calculated energy levels as a function of the electric field for the $13f$ states.

In Figure (6.2) a Starkmap of the $13f$ levels is plotted. The 10 groups can be identified at 4000 V/cm. At 1800 V/cm the peaks are also separated but compared to the zero field separation of $l>4$ levels the separation is fifty times larger. For decreasing principal quantum number this ratio becomes less and zero field positions become more critical. For the determination of small electric fields (<400 V/cm) one can imagine examining the middle plots in Figures (6.1,6.2) this is critical.

Improvements can be made by obtaining zero field spectra. This could be done in two ways. First it could be considered to measure three photon transitions from the ground to the g-states. The calculation will improve if quantum defects of these levels are known. The second possibility is obtaining xenon excitations in a zero field environment. This would determine the starting positions of the f-levels further improving the calculation.

6.1.2 Intensities of the Transitions

The calculation procedure assumes that the energy levels of xenon can be described using the j-K coupling scheme. There is some evidence that this is not completely valid. For example, there are some d-states that do not conform to j-K coupling [34, 31]. The observation of excellent agreement in the positions of the spectral peaks for higher n indicates that this is not a significant problem when estimating Stark effects for the f-levels. It could however affect the calculated intensity distribution. This is a possible reason for the differences in observed and calculated intensities. For calculations involving p and d levels, this might be a larger problem, and must be considered for the 2+1 photon scheme, which involves excitation to d states.

6.2 Spatial Resolution

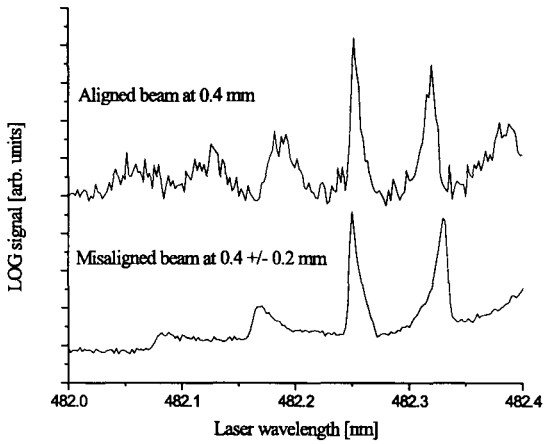

Fig. 6.3: Influence of spatial misalignment of laser beam to excitation spectrum.

A problem indicated in the previous section is poor spatial resolution. In order to check how poor spatial resolution is converted to the spectra the laser beam was misaligned to be not parallel to the electrode. This meant that the beam was passing through regions with varying electric field, and so in the obtained spectrum an electric field distribution should be visible (Figure (6.3)). The observed peaks broaden and become asymmetric [15] ,because in the detection volume an distribution in the electric field strength is observed. With the beam aligned parallel to the electrode this effect is minimized. However, even when the beam was properly aligned with respect to the electrode, spectra indicating zero electric field could not be observed. This indicates that even when the laser was aligned to be far from the electrode, some beam passed through regions with high electric field.

This effect can have several causes illustrated in Figure (6.4).

A The laser beam produces scattered light while entering the vacuum chamber. If this scattered light, with sufficient intensity to excite, passes through an volume with electric field this will produce a LOG signal. The background LOG signals discussed in the previous section could be an indication for this. Reflection and scattering of the exit window of the chamber could cause problems in spatial resolution. In the experiments described in the previous chapter the beam was deliberately aligned so that the reflections did not pass through the discharge. However, this did not solve the spatial resolution problem.

B The influence of the edge of the electrodes causes large electric fields to be measured far from the electrode surface.

C The beam is bigger then expected.

Because the main cause of the spatial resolution problem is related to the experimental arrangement several adjustments can be considered. For example changing the entry and exit windows from flat to Brewster windows, would minimize the chances of reflection and or scattering of the laser beam. Also adding some apertures inside the chamber would improve this problem.

All the possible causes of the poor spatial resolution arise because the LOG signal is generated by the entire laser beam as it passes through the plasma. Fundamentally improving the spatial resolution

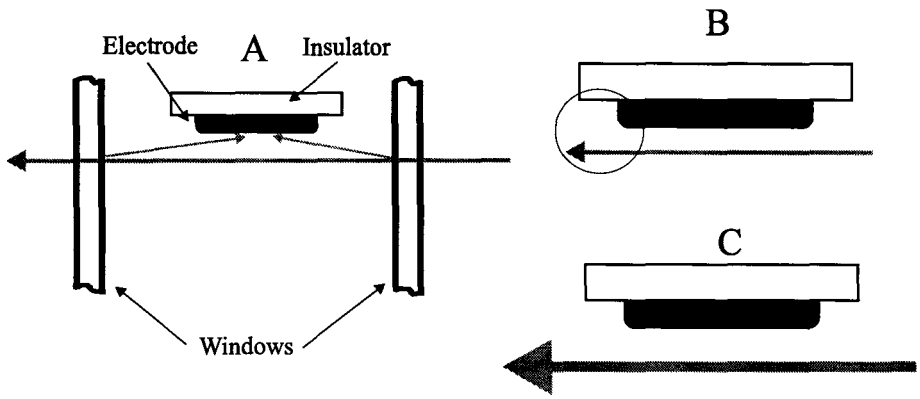

Fig. 6.4: Illustration of the possible cause for poor spatial resolution. (A) Reflections and or scattering of the laser beam. (B) Electrode edges. (C) Large beam.

requires transition to a laser induced fluorescence method, because the spatial resolution in an LIF experiment is determined by the detection optics, and not the laser beam. In chapter four collisional induced fluorescence was expected from the one photon scheme, but this was not observed. This could be caused by a low collision frequency and therefore no collisional redistribution. At higher pressures this problem could be solved. A second cause could be the large number of quenching paths available in xenon.

The application of the 2+1 photon scheme can solve the spatial resolution problem. Thereto a two photon excitation is needed from the ground state to an intermediate level.

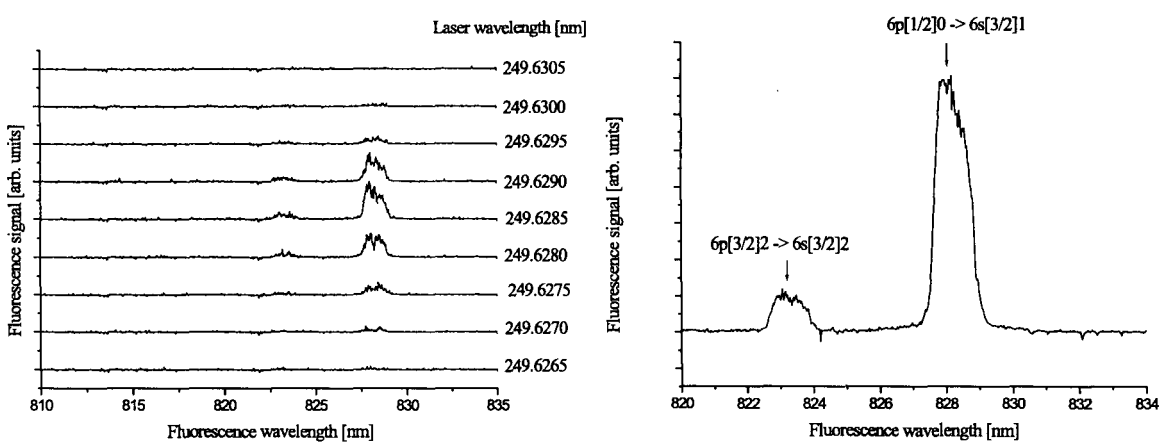

Fig. 6.5: The fluorescence signal for two photon excitation from the ground to the $6p[1/2]_0$ state of xenon. The position with maximum fluorescence is shown in the corner.

In Figure (6.5) the emission around 828 nm is shown as a function of the laser wavelength. The gate width was set at 150 ns. As the laser was scanned across the wavelength corresponding to two-photon excitation from the ground state to the $6p[1/2]_0$ level. Some part of the excited population is redistributed, which results in the additional fluorescence at 823 nm. This shows that a laser induced fluorescence scheme is possible. By using such a scheme, good spatial resolution will be obtainable.

Chapter 7

General Conclusion

The aim of the research was to develop a diagnostic method to measure electric field strength in a gas discharge with spatial and temporal resolution to study micro discharges. From the discussion in the previous chapter several conclusions can be made.

- Stark dependencies can be calculated for xenon and resulting excitation spectra have excellent agreement with experimental spectra.
- In situ electric field measurements can be made with the one photon excitation scheme by using Stark spectroscopy of xenon atoms.
- The 2+1 photon excitation scheme is achievable and the spatial and temporal resolution will be sufficient for micro discharge electric field diagnostics.

The general conclusion is that an in situ electric field diagnostic using xenon Stark spectroscopy is developed and in the future can be applied to study micro discharges.

Acknowledgements

I would like to thank all the people involved from the EPG group, Rina, Wouter, JeanCharles, prof. Dahiya, Nandini, Carole, Gabriela, Jérôme, Wijnand, Hans, Nathalie, Erik W., Erik K., Joost, Mikhail, Eva, Winfred, Eddie, Sharon, Leon, Gerjan and Marcel for their support and useful discussions. The great support from our technicians Loek, Lambert, Charlotte, Huib and Evert is gratefully acknowledged. Especially I would like to thank Jaap for his continuous involvement in making the set-up work. Also the people involved from the ETP group are acknowledged for their cooperation. The efforts from the people from the faculty and glass workshop are greatly appreciated as well as support from Philips by Daiyu Hayashi, Gero Heusler and John Gielen.

I am very grateful to be given the opportunity, to learn from, and work with Mark Bowden and receiving the full support and freedom from Gerrit Kroesen to complete this work.

Bibliography

[1] G. J. M. Hagelaar, *Modeling of microdischarge for display technology*, Thesis, Eindhoven University of Technology (2000).

[2] M. H. Cho, C. Chan, N. Hershkowitz, T. Intrator, *Measurement of vacuum space potential by an emissive probe*, Rev. Sci. Instrum., vol. **55**, 631 (1984).

[3] E. Y. Wang, N. Hershkowitz, T. Intrator, C. Forest, *Techniques for using emitting probes for potential measurement in rf plasmas*, Rev. Sci. Instrum., vol. **57**, 2425 (1986).

[4] L. Windholz, B. Schuh and T. Neger, *Experimental Investigation of the Stark Effect of the Level Groups 7p, 6p' and 6d of Neutral Xenon*, Physica Scripta, vol. **54**, 85 (1996).

[5] R. D. Knight, Liang-guo Wang, Stark-induced 6s-6d transistions in xenon, Phys. Rev. A, vol. **32**, 2751 (1985).

[6] J. P. Booth, J. Derouard, M. Fadlallah, N. Sadeghi, *Time-resolved electric-field measurements in 30 kHz hydrogen discharges by optical emission Stark spectroscopy*, J. Appl. Phys., vol **74**, 862 (1993).

[7] C. A. Moore, G. P. Davis, R. A. Gottscho, *Sensitive, nonintrusive, in-situ measurement of temporally and spatially resolved plasma electric fields*, Phys. Rev. Lett., vol **52**, 538 (1984).

[8] J. Derouard, H. Debontride, T. D. Nguyen, N. Sadeghi, *Time resolved Stark spectroscopy in* $NaK(B^1\Pi; V = 1 - 14)$*. Measurement of permanent electric dipole, radiative lifetimes, and collisional rate constants*, J. Chem. Phys., vol **90**, 5936 (1989).

[9] D. K. Doughty, J. E. Lawler, *Spatially resolved electric field measurements in the cathode fall using optogalvanic detection of Rydberg atoms*, Appl. Phys. Lett., vol **45**, 611 (1984).

[10] J. P. Booth, M. Fadlallah, J. Derouard, N. Sadeghi, *Electric field measurements in discharges by 2+1 photon laser Stark spectroscopy pf atomic hydrogen*, Appl. Phys. Lett., vol **65**, 819 (1994).

[11] K. E. Greenberg, G. A. Hebner, *Electric-field measurement in 13.56 Mhz helium discharges*, Appl. Phys. Lett., vol **63**, 3282 (1993).

[12] G. A. Hebner, K. E. Greenberg, M. E. Riley, *Electric fields in high frequency parallel plate helium discharges*, J. Appl. Phys., vol **76** 4036 (1994).

[13] M. Fadlallah, J. P. Booth, J. Derouard, N. Sadeghi, *Sheath electric field oscillation and ion kinetics in radio-frequency discharges*, J. Appl. Phys., vol **79**, 8976 (1996).

[14] Y. W. Choi, M. D. Bowden, K. Muraoka, *Electric field measurements in an argon glow discharge using laser spectroscopy*, Appl. Phys. Lett., vol **69**, 1361 (1996).

[15] V. P. Gavrilenko, H. J. Kim, T. Ikutake, J. B. Kim, Y. W. Choi, M. D. Bowden and K. Muraoka, *Measurement method for electric fields based on Stark spectroscopy of argon atoms*, Phys. Rev. E, vol. **62**, no. 5, 7201 (2000).

[16] M. L. Zimmerman, M. G. Littman, M. M. Kash, D. Kleppner, *Stark structure of the Rydberg states of alkali-metal atoms*, Phys. Rev. A, vol. **20**, no. 6, 2251 (1979).

[17] V. P. Gavrilenko, H. J. Kim, T. Ikutake, J. B. Kim, M. D. Bowden, K. Muraoka, *Method to measure electric field vector in an argon glow discharge using laser polarization spectroscopy*, Phys. Rev. E, vol **63**, 047401 (2001).

[18] U. Czarnetski, D. Luggenholscher, H. F. Döbele, *Sensitive electric field measurement by fluorescence dip spectroscopy of Rydberg state of atomic hydrogen*, Phys. Rev. Lett., vol. **81**, no. 21, 4592 (1998).

[19] B. Chapman, *Glow Discharge Processes*, John Wiley & Sons, New York (1980).

[20] A. Goehlich, T. Kawetzki, H. F. Döbele, *On absolute calibration with Xenon of laser diagnostic based on two photon absorption*, J. Chem. Phys., vol. **108**, 9362 (1998).

[21] N. Sternberg, V. A. Godyak, *Approximation of the bounded plasma problem by the plasma and the sheath models*, Physica D, vol. **97**, 498 (1996).

[22] R. D. Knight, Liang-guo Wang, *Stark structure in Rydberg states of xenon*, Phys. Rev A, vol. **32**, no. 2, 896 (1985).

[23] A. R. Edmonds, J. Picart, N. Tran Minh, R. Pullen, *Tables for the computation of radial integrals in the Coulomb approximation*, J. Phys. B, vol **12**, 2781 (1979).

[24] M. D. Bowden, V. P. Gavrilenko, *Stark spectroscopy simulations*, private communication (2001).

[25] J. H. R. Feijen, *Electronic design of LOG circuit*, private communication (2001).

[26] B. N. Ganguly, A. Carscadden, *Electric field vector measurement in a glow discharge*, Phys. Rev. A, vol **32**, 2544 (1985).

[27] B. N. Ganguly, *Measurement of high Rydberg* ^1P *spectra of atomic heliom and its application to glow-discharge diagnostics*, J. Appl. Phys., vol **60**, 571 (1986).

[28] B. N. Ganguly, J. R. Shoemaker, B. L. Preppernau, A. Garscadden, *Rydberg state Stark spectroscopic measurement of electric field profile in a glow discharge*, J. Appl. Phys., vol **61**, 2778 (1987).

[29] M. P. Alberta, H. Debontride, J. Derouard, N. Sadeghi, *Space and time resolved electric field vector distribution in radiofrequency discharges between unequal area electrodes*, J. Phys. III France, vol **3**, 105 (1993).

[30] E. E. Salpeter, H. A. Bethe, *Quantum mechanics of one- and two-electron atoms*, Springer (1957).

[31] A. R. Striganov, N. S. Sventitskii, *Tables of spectral lines of neutral and ionized atoms*, (1968).

[32] M Ahmed, MA Baig, B Suleman, *Laser optogalvanic spectroscopic studies of xenon*, J. Phys. B: At. Mol. Opt. Phys. **31**, 4017-4028 (1998).

[33] Liang-guo Wang, R. D. Knight, *Two-photon laser spectroscopy of the ns' and nd' autoionizing Rydberg series in xenon*, Phys. Rev. A, Vol. **34**, no. 5, 3902-3907 (1986).

[34] R. D. Knight, Liang-guo Wang, *Stark structure in Rydberg states of xenon*, Phys. Rev. A, Vol. **32**, no. 2, 896-900 , (1985).

[35] P. Labastie, F. Biraben, E. Giacobino, *Optogalvanic spectroscopy of the ns and nd Rydberg states of xenon*, J. Phys. B: At. Mol. Phys. **15**, 2595-2603 (1982).

[36] M. Hanif, M. Aslam, Raheel Ali, Ali Nadeem, M. Riaz, S. A. Bhatti, M. A. Baig, *Laser optogalvanic spectroscopy of 5p5nf J=1-5 even-parity Rydberg levels of xenon*, J. Phys. B: At. Mol. Opt. Phys. **33**, 4647-4655 (2000).

[37] R. D. Knight, Liang-guo Wang, *One-photon laser spectroscopy of the np and nf Rydberg series in xenon*, J. Opt. Soc. Am. B, vol. **2**, no. 7, 1084-1087, (1985).

Appendix A

Technology Assessment

Discharge or plasma technology has become important in everyone's life. As stated in the introduction the kind of plasma discussed in this master thesis has many applications. The application of glow discharges range from plasma television to maybe in the future, biomedical treatments.

Scientific knowledge of plasmas is directly related to the fact if parameters can be measured. Electric field is the fundamental force from which the plasma gains its energy. Studying the behavior of electric field in plasma could generate new insights in plasma physics. For example electric field measurements during breakdown of a gas could provide some new interesting results.

The non equilibrium micro plasma has not been studied very well experimentally, because there are almost no diagnostic tools. The main limiting factors have been time and spatial resolution. Technology advancements in laser and imaging techniques offer the possibility to explore micro plasma experimentally. The parameters of the micro plasma need to be obtained in order to improve or even create micro plasma technology.

One of the first micro plasma technologies which is available on the commercial market is the plasma television. The micro plasma in each pixel of the television contains xenon and neon. A major problem is the energy loss caused by the micro plasma's electric field. Developing a diagnostic being able to measure the electric field in such a micro plasma benefits science as well as technology. The technology of micro plasma improves and a diagnostic tool becomes available for future plasma research.